

AC Loss Modeling of Superconducting Field Windings for a 10MW Wind Turbine Generator

an Analytical and Numerical Analysis

J. Schellevis

Master of Science Thesis

AC Loss Modeling of Superconducting Field Windings for a 10MW Wind Turbine Generator

an Analytical and Numerical Analysis

MASTER OF SCIENCE THESIS

For the degree of Master of Science in Sustainable Energy Technology
at Delft University of Technology

J. Schellevis

Supervisors:
dr.ir. H. Polinder
ir. D. Liu

September 21, 2014

Abstract

The total installed capacity of wind turbines is growing as society moves towards a more sustainable energy supply. With the integration of more wind turbines in the grid the price and reliability of future wind turbines are very important. One of the promising drive train topologies currently investigated is the direct drive superconducting wind turbine. This configuration allows for higher reliability, less top mass and nearly full independence of the volatile market of rare earth metals. However, the superconducting windings in such a generator operate only at cryogenic temperatures which is a challenge in the design of the machine.

Since superconducting windings operate at a very low temperature it is important to estimate the heat generation in the windings. AC loss is the main cause of heat generation in a superconducting field winding. This thesis attempts to analyse the AC loss in two 10MW superconducting generator designs using analytical and numerical modeling. After introducing the problem description, the theory concerning AC loss in superconducting wires is treated. Then, the methods for both modeling techniques are established and partly validated. The results are then shown and discussed after which the conclusions are drawn. Both generators are designed for the same turbine and therefore have the same rotational speed and rated power which makes them comparable. The geometry however is different and as the results will show, these differences in design result in major differences in AC loss. Depending on machine geometry the analytically calculated AC loss is ranging from 22.2W to 283W in the Non Magnetic Teeth (NMT) design and 0.7kW to 2.9kW in the Iron Teeth (IT) design. The numerically calculated hysteresis loss is on average 154W in the NMT machine and 371W in the IT machine.

Table of Contents

Table of Contents	iii
List of Figures	v
Glossary	vii
List of Acronyms	vii
List of Symbols	vii
Acknowledgements	xi
1 Introduction	1
1-1 Superconducting Wind Turbine	1
1-2 The INNWIND Project	2
1-3 AC Loss in Superconducting Generators	3
1-4 Problem Statement	4
1-5 Contribution to Literature	5
1-6 Overall Procedure and General Assumptions	5
1-7 Thesis Structure	6
2 Theoretical Background	7
2-1 History of Superconductivity	7
2-2 Application of Superconductors	9
2-3 Properties of Superconductors	10
2-4 The Bean Model	11
2-5 Extended Bean Model	12
2-6 Effect of Transport Current	12
2-7 AC Loss in a Superconductor	14

2-8	Analytical Calculation of AC Loss in Multifilamentary Superconductors in Transverse Field	17
	Cylindrical Filaments in Slowly Changing Transverse Magnetic Field	18
	Rectangular Filaments in Slowly Changing Parallel Magnetic Field	22
	Merged Filaments in Rectangular Shape	22
2-9	Numerical Modeling of Superconductors	23
2-10	Loss Calculations in the Frequency Domain	24
2-11	Time and Space Harmonics	25
3	Research Methods	27
3-1	General Approach	27
3-2	Analytical Methodology	29
	Magnetic Field Modeling	29
	Amplitude and Frequency Calculation	29
	Relative Penetration Field and AC Loss Calculation	33
	Volume Averaging	33
3-3	Experimental Validation of Analytical Methodology	34
3-4	Numerical Methodology	36
4	Results and Discussion	39
4-1	Magnetic Field Distribution	39
4-2	AC Field due to Space Harmonics	41
4-3	AC Field due to Time Harmonics	43
4-4	AC Loss in the Field Winding	45
5	Conclusions and Recommendations	49
5-1	Conclusions	49
5-2	Recommendations	51
	Bibliography	53
	A Assignment with Experimental Data	57
	B Data Extraction for Numerical Model	65
	C Example of Publication	67

List of Figures

1-1	Cross section of superconductor wire with Magnesium diboride (MgB_2) filaments embedded in a Nickel matrix and supported by a Copper stabilizer strip on top [1] and a single racetrack coil.	3
2-1	Kamerlingh Onnes's graph showing the electrical resistance of mercury at low temperatures [2].	8
2-2	Meissner effect in superconductors as the conductor is above (left) or below (right) the critical temperature in a constant magnetic field, below H_1 [3].	9
2-3	Plot of voltage versus current at $T = 4.23\text{K}$ and $B = 5\text{T}$ on NbTi filamentary conductors of large (high values of n) and small (low values of n) diameter filaments [4].	11
2-4	Penetration of magnetic flux into the cross-section of a superconducting slab. Induced currents are represented by the arrows going in and out of the plane of view. The field, H_a , is increasing up to full penetration (a-c) and reduces again (d) [5].	11
2-5	Magnetic field penetration profiles within a superconducting slab in a perpendicular field of: (a) small amplitude, (b) penetration amplitude and (c) high amplitude.	12
2-6	Critical current surface for an alloy of niobium-titanium [6].	13
2-7	Magnetic field penetration profiles within a superconducting slab carrying a transport current and exposed to an external perpendicular AC field of: (a) small amplitude, (b) penetration amplitude and (c) high amplitude.	13
2-8	Hysteresis loss in a slab carrying a transport current in a parallel AC field. β is the ratio between the field amplitude H_0 and the penetration field H_p and Γ is the fraction of energy loss compared to the total amount of energy that is supplied via the AC field [7].	14
2-9	Schematic representation of types of loss occurring in a superconducting wire. Numbers in the cross-section represent: 1 hysteresis loss, 2 eddy current loss, 3 coupling loss and 4 ferromagnetic loss.	15
2-10	Current penetration in coupled and uncoupled filaments in a changing transverse magnetic field. The red and blue regions correspond to a current in and out of the plane. The arrows indicate the direction of the magnetic field which has reached the maximal value at the displayed time.	16

2-11	Scenarios that approximate the real wire with simplified geometries, visualised by projection of assumptions on wires cross-section.	18
2-12	Current penetration in a cylindrical conductor filament with transverse applied field and the penetration depth w and w_0 as function of the angle θ	18
2-13	Resistivity digram of Cu-Ni alloy for varying compositions at 20K [8]	20
2-14	B-H curves of two samples of nickel films showing hysteric behaviour. The left curve is a well-annealed nickel wire and the right curve is a unannealed sample of the same wire [9].	21
2-15	2d mesh of a pole pair with a very fine mesh near the air-gap.	24
2-16	The MMF in the airgap of a typical 3-phase electrical machine [10].	26
3-1	Cross-section of one pole pair of the NMT and IT generator designs with the iron (yellow), armature winding (orange), field winding (red) and center of air gap (blue), representing the boundary between rotating and static reference frames. White indicates non ferromagnetic material.	28
3-2	Flowchart of analytical methodology	30
3-3	Radially sampled field winding by 10 curves ranging from $R=2.505m$ till $R=2.595m$	31
3-4	Result of selection of dominant frequency by equation	32
3-5	Theoretical and experimental AC loss of NbCu7-ODS wire. The symbols are measurements and the lines are calculated [11]	34
3-6	Cross section of the multifilamentary wire used in the experiment, the magnetization loop measured at 4.2K when flux density is changed between 1 and 3T with a frequency of 2mHz and the theoretical and experimental loss per frequency of MgB2 wire 2163.	35
3-7	The four boundaries of the field windings at which the magnetic field distribution is copied from the 'field' model to the 'superconductor' model.	36
4-1	Surface plot of Magnetic flux density in the non-magnetic and iron teeth machine at maximal torque	40
4-2	Magnetic flux density throughout the field winding. Each group of lines is taken at different radius in the field winding (Figure 3-3). The width of each group of lines represents the field change in time.	41
4-3	AC component of magnetic flux density in the field winding at the largest radius and maximal torque.	42
4-4	Relative penetration field β as function of the position angle in the field winding at the smallest radius in the field winding.	43
4-5	Result of frequency selection applied on IT machine at max torque, radius of $R=2.4595m$ and $\beta > 1$	43
4-6	Armature current waveform and frequency spectrum at rated operation	44
4-7	Analytically calculated hysteresis loss per unit volume of the cylindrical filament scenario throughout the field winding cross-section	46
4-8	AC loss components in the full machine as function of the torque. Hysteresis loss is displayed per scenario. Eddy current loss and coupling loss are not influenced by the various scenarios or relative penetration field.	47
4-9	The average dominant harmonic frequency over the field winding in the IT machine.	48

Glossary

List of Acronyms

CoE	Cost of Electricity
CoP	Coefficient of Performance
EM	Electro Magnetic
FEM	Finite Element Method
IT	Iron Teeth
MgB₂	Magnesium diboride
MRI	Magnetic Resonance Imaging
NMT	Non Magnetic Teeth

List of Symbols

α	Constant used in extended Bean model
α_s	Field winding sector angle
β	Relative magnetic penetration
δ	Skin depth
γ	Power factor for E-J curve
\hat{H}	Amplitude of magnetic field strenght
κ	Dominant frequency indicator
λ	Superconductor fill factor
λ_{fer}	Ferromagnetic fill factor
μ_r	Relative permeability
ω	Rotational speed

\overline{P}_c	Average coupling power loss
\overline{P}_e	Average eddy current power loss
\overline{P}_f	Average ferromagnetic power loss
\overline{P}_h	Average hysteresis power loss
\overline{P}_{AC}	Average AC power loss
ρ	Resistivity
σ_{\perp}	Perpendicular conductivity
σ_m	Conductivity of matrix material
σ_{nm}	Conductivity of normal metal
τ	Armature slot/teeth width ratio
θ	Position angle in cylindrical superconductor
a	Radius of circular wire or half the thickness of rectangular wire
a_0	Wire radius
A_{sup}	Cross sectional area of superconductor
B_0	External applied magnetic flux density
B_{ex}	Constant used in extended Bean model
C_c	Constant factors of coupling loss combined
C_e	Constant factors of eddy current loss combined
C_h	Constant factors of hysteresis loss combined
d_a	Armature winding thickness
d_f	Field winding thickness
d_y	Yoke thickness
d_{EM}	EM shield thickness
E	Electric field strength
E_0	Electric field constant
f	Frequency
F_s	Sample frequency
H	Magnetic field strength
h	Family of space harmonics
H_0	External applied magnetic field strength
H_1	Magnetic field strength at which the magnetic field starts to penetrate
H_2	Magnetic field strength at which superconducting properties are lost
H_c	Critical magnetic field strength
H_p	Magnetic field strength at full penetration i.e. penetration field
i	Relative transport current
I_c	Critical current
I_t	Transport current
j_c	Critical current density
j_t	Transport current density
K_h	Constant of ferromagnetic loss depending on volume and material

L	Filament twist pitch length
n	Exponent of ferromagnetic loss
R	Radius
R	Radius
r_y	Yoke inner radius
r_{a1}	Armature winding inner radius
r_{f1}	Field winding inner radius
r_{r2}	Rotor outer radius
r_{s1}	Stator inner radius
T	Temperature
t	Time
T_c	Critical temperature
t_p	Time of rotation of one pole
V	Volume
w	Penetration depth
w_0	Maximal Penetration depth
w_r	Width of rectangle
m	Positive integer
p	Number of pole pairs

Acknowledgements

During this thesis, I received contributions, suggestions and encouragement from fellow students, supervisors and family. I am especially thankful to Henk Polinder for guiding me into this thesis and the feedback during the process. Also I am thankful to Dong Lui, who has been in close contact with me and the project. He has helped a lot in steering this thesis in the right directions with our weekly discussions in the progress meetings. I want to thank the EPP research group, especially Martin van der Geest for his contribution and support regarding the data extraction from Comsol.

I also want to thank two persons from other universities whom I have met in the process of gathering information. First, Prof. dr. Herbert de Gerssem, from KU Leuven, who taught me new numerical modeling techniques and provided a lot of insight in the problems involved. Second, Dr. Marc Dhallé, researcher and teacher at the University of Twente, who supplied the experimental data which was very useful.

Most of the time was spent in the EPP student room which I found very pleasant due to the company of my fellow students: Einar, Foivos, Nikos, Jose Ralino, Didier, JK, Udai, Nikos and Lafelli. Finally, I want to show my gratitude to Leontien for her continues support and encouragement during the course of this thesis. Without her support this project would have been much more stressful.

Delft, University of Technology
September 21, 2014

J. Schellevis

Chapter 1

Introduction

To understand AC loss in superconducting generators, knowledge of electrical and magnetic loss mechanisms, superconductivity and electrical machines is needed. Therefore this introduction provides a short introduction to these fields of work and a good understanding of the problems at hand.

1-1 Superconducting Wind Turbine

Ever since the development of the first electricity producing wind turbine the constant trend has been to increase the size and power output of a single turbine. The largest wind turbine commercially available nowadays is equipped with a rotor diameter of 164m and has a rated power of 8MW [12]. The main driver of this trend is the Cost of Electricity (CoE) because, the CoE is lower as wind turbines get larger. Especially in offshore wind energy the CoE needs to be reduced in order to compete with electricity generation from fossil fuels.

Scientific research is usually about 10 years ahead of commercially available wind turbines. One of the technologies currently being researched is the superconducting wind turbine. Details about superconductivity are explained in Chapter 2, for this chapter it is sufficient to know the difference between a superconducting and conventional electrical machine.

A conventional electrical machine has copper windings to create a set of magnetic fields which interact with each other. The strength of these magnetic fields is depending on the current density in the winding, so a larger current density results in stronger magnetic fields. However, the current in a copper winding is also prone to resistive losses which cause the windings to heat up. The current density is limited due to the maximal temperature thus, additional methods are used to increase the magnetic flux density. The magnetic path in an electrical machine is usually made out of low reluctance ferromagnetic material like cast iron, to concentrate the magnetic field lines and increase the magnetic flux density without increasing the heat generation in the winding. The torque produced by an electrical machine is depending on three parameters: the magnetic flux density, the radius and length of the machine e.g. a higher field strength or larger machine can generate a higher torque.

All ferromagnetic materials experience magnetic saturation which is one of the limitations of a conventional electrical machine. Cast iron for example starts to show the effect of saturation around a flux density of 0.8T by a non-linear increase of the flux density with the applied magnetic field strength. Due to iron saturation the air-gap flux density in conventional electrical machines is usual kept below 2T. Higher flux densities are possible but will come at the expense of much higher current i.e. resistive loss. So, to increase the torque of a conventional electrical machine, the volume needs to increase which is a drawback especially for wind turbine applications since with the volume also the weight and price of the generator increase.

The superconducting windings of a superconducting generator can conduct a large current density without any measurable loss. However, these windings are only superconducting at cryogenic temperatures, which is in this project at 20K. The benefit of a superconducting winding is the very high flux density, up to 25T [13] at the expense of nearly no loss. A large flux density removes the need for ferromagnetic materials and thus removes the limiting magnetic saturation and makes the machine lighter. A superconducting electrical machine is much smaller and lighter compared to a conventional electrical machine of the same power rating. Since the generator of a wind turbine is positioned in the nacelle, on top of the tower, A smaller and lighter generator means a lighter tower and nacelle construction i.e. with less material costs, reducing the CoE. An other advantage of a superconducting generator is the independence of the rare earth materials. The prices of these materials is very unstable due to the limited number of suppliers. Minimizing the use of rare earth materials removes a major uncertainty in material costs.

In the field of superconducting electrical machines there are two main concepts designed. The first concept is a fully superconducting electrical machine in which the armature and field windings are both superconducting. The other concept is a partially superconducting electrical machine where only a superconducting field winding is used in combination with a conventional armature winding. Also, the type of superconductor is varied since each superconductor seems to have benefits and drawbacks. Which concept and material is optimal to use is still unknown and that already shows the technology is still in an early phase of research. One of these research projects is the INNWIND project.

1-2 The INNWIND Project

This thesis is contributing to the international research project named INNWIND. Funded by the European Union's Seventh Framework Programme for research, the INNWIND project is exploring the design of a state-of-the-art 10-20MW offshore wind turbine. The project is a collaboration between 27 participants from all over Europe containing Universities, Governmental research centres and private owned companies active in the wind turbine industry. The project is divided into work packages and The Electrical Power Processing (EPP) group at Delft University of Technology is taking part in the 'Electro-Mechanical Conversion' work package. Among others this package contains the design of the superconducting direct drive generator (Task 3.1) and specifically Subtask 3.1.1, investigating various superconductor materials and cooling systems [14] which is the framework of this thesis.

The advantage of a large project like INNWIND is that a lot of decisions already have been made, for instance: the mechanical design of the machine, the rated power range, the rota-

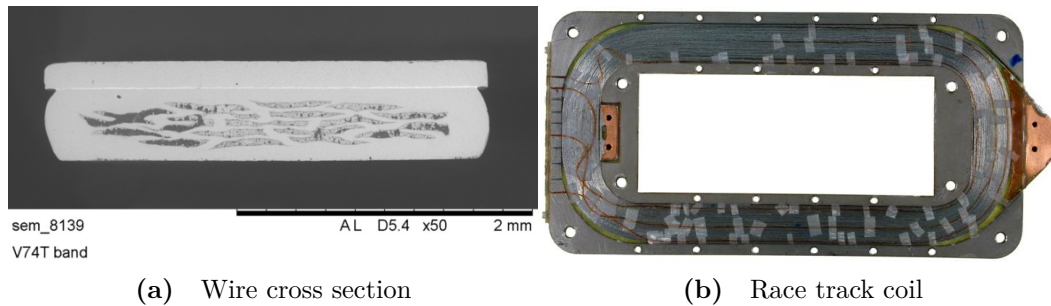


Figure 1-1 Cross section of superconductor wire with MgB_2 filaments embedded in a Nickel matrix and supported by a Copper stabilizer strip on top [1] and a single racetrack coil.

tional speed and the operational temperature of the superconducting windings. Additional boundaries are assumed in order to limit the size of this project. The general assumptions or limitations are listed in Section 1-6.

One of the important boundaries set by the framework is the superconductor type and design of the wire. In collaboration with a producer of superconducting wires the design of a Magnesium diboride (MgB_2) wire with the cross section shown in Figure 1-1a is used. The thickness and width of the wire is 0.7mm and 3mm. The center contains 19 filaments of MgB_2 embedded in a nickel matrix and a single sided copper stabilizer strip is added. This wire is wound in the shape of a racetrack coil of which an example is shown in Figure 1-1b and several coils are combined to make up the total field windings of the generator.

The INNWIND project investigates multiple generator designs which are all optimised for lowest CoE. Two of these designs are used in this thesis: 1) a Non Magnetic Teeth (NMT) machine containing a light composite non magnetic material in between the armature windings and 2) an Iron Teeth (IT) machine where iron teeth are used in the armature to concentrate the magnetic flux density. The active material in the IT machine has a total mass of 105ton and a combined price of 1300k€. Although with 99ton the weight of the NMT machine is less, the total price of the active material is 1700k€.

1-3 AC Loss in Superconducting Generators

Before the problem statement is given, a very short introduction to AC loss is given. The title of this thesis already shows this research is evaluating AC loss, but what is considered as AC loss and where does AC loss origin from in electrical machines? It is well known that 'AC' is the abbreviation for Alternating Current. However, in the field of AC loss, the abbreviation 'AC' is usually referring to more than alternating current. The definition of AC loss in this thesis is all loss generated in a superconducting wire, including the non-superconducting parts of the wire, originating from time varying currents and/or magnetic fields.

In field windings of electrical machines time varying currents are caused by change of operational point i.e. changing excitation, and by the power supply electronics connected to the field winding. Time varying magnetic fields in the field windings of a synchronous electrical machine are mainly caused by non sinusoidal distribution of armature windings and armature power electronics. The magnetic field changes due to non sinusoidal armature winding

distribution is referred to as space harmonics and magnetic field changes due to a non sinusoidal current waveform on the terminals of the generator is referred to as time harmonics. In Chapter 2 more information can be found on AC loss and time and space harmonics.

1-4 Problem Statement

At the start of this thesis a 'Thesis Application Form', including the problem description, is handed in. The quote below is the problem description of this thesis, initially written by Dong Liu and is slightly adapted during the thesis.

In superconducting machines, thermal budgets are very important for the cooling system. AC losses in superconductors are part of the thermal budget, which are difficult to accurately predict. This project aims at modeling of AC losses in MgB₂ superconductor field windings. A survey on the possible methods for calculating the AC losses will be done first, followed by applying the methods on two cost-optimised designs of a 10MW superconducting wind turbine generator. The winding design will then be modelled in numerical way to predict the AC loss due to various magnetic field harmonics.

Predicting and optimizing the AC loss in a superconducting electrical machine is very important since the design of the cryogenic cooler is depending on the loss in the windings. In a superconducting generator, the windings are cooled down to very low temperatures in order to make the material superconducting. MgB₂ enters the superconducting state at a temperature of 40K [15] but usually the operational temperature is lower. Cooling requires a lot of energy due to the low efficiency of a cryogenic cooler which is usually expressed as a Coefficient of Performance (CoP). The theoretical maximal CoP of a cooler removing heat from 20K and rejecting heat at 293K is 0.0733. This means for one unit of energy put into the system, 0.0733 units of heat are removed at 20K. Or put differently, the removal of 1J of heat at 20K requires nearly 14J of energy. In addition, the real CoP of a cryogenic cooler is usually much lower than the theoretical maximum hence even more energy is needed to remove 1J of loss in the windings.

The main research question is: How large is the AC loss in the field windings of two designs of a 10MW superconducting generator? To structure this research the following sub-questions are formulated.

1. What are the basics of superconductivity?
2. Analytical calculation
 - (a) Which AC loss mechanisms exist?
 - (b) Which AC loss mechanisms and factors are relevant for this study?
 - (c) How can each relevant loss mechanism be analytically calculated?
3. Numerical calculation
 - (a) Which numerical method is most suited for this study?

4. Methodology

- (a) Which methodology will be applied for the analytical calculations?
- (b) Which methodology will be used for the numerical calculations?

5. Validation

- (a) How does the analytical methodology perform in comparison to experimental results?

1-5 Contribution to Literature

Research on superconductor technology is currently going on for more than a century. For example, large contributions have been made by scientist Dr C.P. Bean and Dr A.M. Campbell in the past, and more recent on going research by F.Grilli and N.Amemia which together are responsible for over 60 scientific publications in the last decade on superconductivity and AC loss [16].

There are numerous papers validating the AC loss theories with experimental work [17] [18] [19]. Each publication varies in superconductor material, wire geometry, frequency range and field amplitude of the validation. This project contributes to the literature on AC loss in superconductors by applying the established theories on the application of the partly superconducting electrical machine of 10MW with low rotational speed. Additionally the result is validated with experimental results of a multi filamentary MgB₂ wire in the frequency range of 0Hz to 20mHz and a magnetic flux density between 1T and 3T.

No scientific literature is found covering multi-frequency AC loss in superconductors. Nearly every publication and theory assumes a single frequency and amplitude to analyse the AC loss. This thesis uses the same theoretical approach applicable for single frequency AC loss calculation and extends this with a method of calculating a surrogate frequency which represents the largest loss contribution and determining the amplitude making the overall method suited for multi-frequency problems.

In this project also the effect of operational point of the generator on the AC loss is studied by varying the output torque from 0Nm (no-load) to maximal torque. This effect, specific for superconducting field windings is not found in literature.

1-6 Overall Procedure and General Assumptions

First the basics of AC loss in superconductors and the theoretical calculation of AC loss in superconductors is explored. Second, the research questions are formulated followed by determining a suited methodology for applying the theory on the superconducting field winding of the two wind turbine generator designs of this project. At the end of the methodology, an experimental validation is added. Then, the AC loss is estimated using the analytical equations as well as numerical modeling of which the results are compared. And finally the results of each step is used to answer the research questions and draw the conclusions.

In general, the following assumptions are made:

- Steady state operation of the generator i.e. constant field or excitation current, constant armature rms-current, constant speed, constant load angle and constant armature frequency.
- Constant rotor speed which is the rated speed of the generator.
- Constant operational temperature of field winding of 20K.
- Critical current density of the superconductor is 1.6043×10^8 A/m² at 20K and 3T.
- Considering 2D model, ignoring end winding losses

1-7 Thesis Structure

This introductory chapter is followed by four more chapters. Chapter 2 is describing the theoretical background related to the problem statement. A short history of superconductivity is given starting at the discovery and ending, in chronological order, at describing the used applications nowadays. Furthermore, the remarkable properties of superconductors are described as they were discovered early in the 20th century. A bit further into the theory the actual loss mechanisms and gradually more mathematical expressions for loss calculations are written down. The third chapter covers the methodology and validation, stating specific assumptions applicable on this project with the used geometries and materials. The results are displayed and discussed in the fourth chapter. This chapter has a general structure of figures showing a result, followed by an explanatory and discussing section taking the reader through all the findings of this project. The fifth and final chapter contains the conclusions and recommendations combining the information from the previous chapters to answer the research questions.

As said, the next chapter begins with describing the history of superconductivity and the first sections are intentionally written in a story-telling manner to make it accessible for readers with different backgrounds.

Theoretical Background

Initially the phenomenon of superconductivity was given the name 'suprageleider' by its discoverer Kamerlingh Onnes in 1911, which translates to 'supra conductor' in English [20]. This chapter will describe much more about the discovery and development of superconductivity. The peculiar properties of superconductors are discussed and the categorization of certain superconductors based on these properties. Additionally, a section will elaborate on the most commonly used theoretical model for superconductors, the Bean model which is widely used to analyse superconductor behaviour, followed by analytical formulas based on the Bean model which could be used to calculate the AC loss in a superconductor in specific conditions.

2-1 History of Superconductivity

The history of superconductivity reaches back more than 100 years from now. It was the Dutch scientist Heike Kamerlingh Onnes who discovered superconductivity in 1911 at his laboratory in Leiden. A few decades earlier in 1882, Kamerlingh Onnes was appointed to the first chair of physics at the University of Leiden. In his laboratory he focused research on liquefying gasses as it was by then already discovered that all gasses could, and had been liquefied with the exception of hydrogen [21]. Unfortunately, for Kamerlingh Onnes, it was Sir James Dewar who was the first to liquefy hydrogen in 1898, aided by the invention of a double-walled insulated container named after him.

Although Kamerlingh Onnes lost the race to be the first to liquefy hydrogen, the research in his laboratory continued. This time with the use of Dewar's cryogenic container he finally managed to liquefy helium in 1908 [22]. It turned out to be extremely complex to continuously produce useful quantities of liquid helium because for the next 15 years, Leiden was the only place in the world that produced liquid helium. Therefore it might not be a surprise that superconductivity was not discovered somewhere else [21].

Three years later the discovery of superconductivity was a fact. By measuring the resistance of a droplet of mercury at the temperature of liquid helium Kamerlingh Onnes and his lab

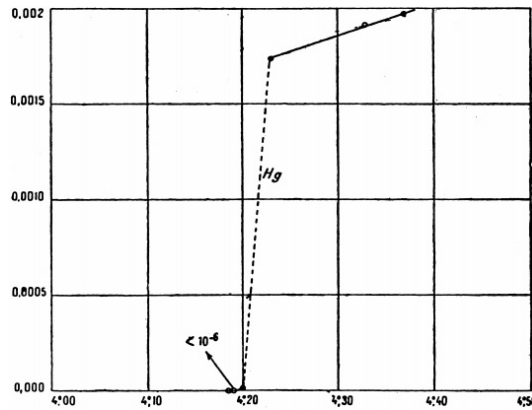


Figure 2-1 Kamerlingh Onnes's graph showing the electrical resistance of mercury at low temperatures [2].

partners noticed the remarkable behaviour of superconductors. In an experiment at a temperature below 4.2K the resistance of the mercury was suddenly so small that it seemed like a short circuit had been made. The measurements showed also that when the temperature rose above 4.2K the resistance of mercury abruptly restored to a measurable value. Figure 2-1 shows the plot Kamerlingh Onnes made based on the measurements done in his laboratory. The resistance of the superconducting state could only be measured up to an accuracy of $10^{-6}\Omega$ so the measurement proved it was less or equal to this value. The steep drop in resistance was very unexpected and much too sudden to be explained by Albert Einstein's theory of quantum oscillators. At that time his theory was thought to explain the way resistance in metals diminished at cryogenic temperatures [23].

Quickly after the discovery of superconductivity it was realized that perfect conductivity would have some consequences for the behaviour of a superconductor. The basics of one of the consequences was founded by Michael Faraday who showed that a changing magnetic field induces a voltage inside a conductor. When a superconductor is treated as a perfect conductor this implies it cannot support a voltage since as can be seen from Ohm's law the current in that case would have to be infinite. This, of course, is not the case and therefore, at time-constant situations, neither a constant electric field nor magnetic field can exist inside a perfect conductor according to Faraday's law. What happens inside a superconductor could be explained by the work of Heinrich Friedrich Emil Lenz, published almost 80 years earlier in 1833. Lenz formulated a law, which was later named after him, that, similar to Faraday, described the interaction between conductors and changing magnetic fields. The Lenz's Law denotes that a changing magnetic field will give rise to a current from which the magnetic field will oppose the original magnetic flux. In the case of a perfect conductor this implies the induced magnetic field will be exactly equal but opposing the external field, resulting in zero field inside the superconductor. Continuing on this line of thought, this also suggests a superconductor is able to trap a magnetic field in the case of cooling it past the critical temperature, the temperature at which it becomes superconducting, in the presence of a magnetic field. Experiments done before the 1930s seemed to show this behaviour of trapping magnetic fields but it turned out these experiments were incorrect [20].

It was the work of Walther Meissner and Robert Ochsenfeld that discovered the second extraordinary property of a superconductor, later only named after the first scientist, the Meissner effect. In 1933 both men performed an experiment that showed the magnetic field

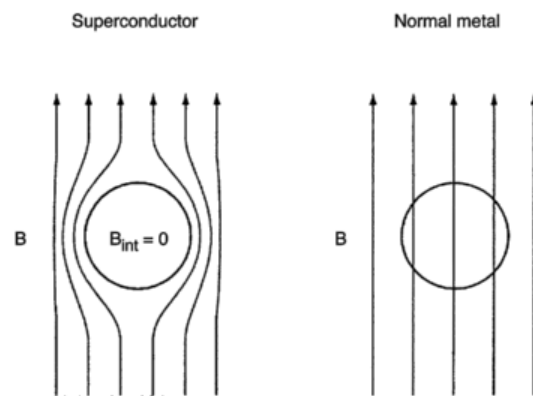


Figure 2-2 Meissner effect in superconductors as the conductor is above (left) or below (right) the critical temperature in a constant magnetic field, below H_1 [3].

was not fixed inside a superconductor when it is cooled down through the critical temperature as described by Lenz' law. Instead, the magnetic field was forced out of the material. Later experiments showed the field was suddenly expelled from the center of the material, forcing the field lines to run around the superconductor as shown in Figure 2-2. The explanation can be found in the surface currents of the superconductor. When the material becomes superconductive, screening currents occur near the surface of the material, screening the inside from the outside magnetic field [20]. This is the case for type-I superconductors which suddenly lose their superconducting properties once the field strength reaches above a certain value H_1 to penetrate.

Then, there are also type-II superconductors which behave the same as type-I superconductor below H_1 but at higher field strengths the flux lines gradually penetrate the material, without losing it's superconducting properties. When the magnetic field reaches above a value marked with H_2 the superconducting properties are lost. The region between H_1 and H_2 can be seen as an transition region from no magnetic field penetration, to full magnetic penetration. Section 2-7 shows that although the flux lines seem to enter the superconducting material, they are still shielded from the superconducting parts by current vortices. This project only focuses on Magnesium diboride (MgB_2) which is a type-II superconductor.

2-2 Application of Superconductors

Ever since the discovery of superconductivity several well known applications have been developed that make good use of the phenomenon. The majority of the applications use coils of superconductors to generate strong magnetic fields since superconductors have the potential to produce large values of high magnetic fields with a small consumption of electric power. Examples of daily used applications are Magnetic Resonance Imaging (MRI) scanners, accelerator magnets, nuclear fusion reactors, magnetic energy storage devices and mid-sized motors or generators in prototype vessel propulsion. These products make use of the very low resistive loss of a superconductor at high current which enables strong magnetic fields, say, of over 25T [13]. As comparison, conventional iron-cored electromagnets operate in a range of up to 2T due to the saturation of the iron at higher fields. Stronger magnetic fields can be produced with normal electromagnets but at the expense of very high power consumption

and the inevitable large amount of required cooling linked to high power consumption [6].

Another daily used product that utilises superconductors is a magnetically levitated train. Although some magnetically levitated trains make use of normal conductive materials or permanent magnets, there are also magnetically levitated trains that make use of superconductors. In this application the Meissner effect is exploited to generate a stable magnetic levitation above the track. Stable levitation at any speed, without the use of an external controller is possible due to the perfect diamagnetic behaviour of the superconductor.

At first glance, one of the most obvious applications of superconductors is their use in high voltage transportation grids. Taking the resistivity out of these systems will eliminate the biggest source of loss in long distance energy transportation. However, currently only small pilot projects have been completed and a true breakthrough into the energy distribution market is still some way off. There are several reasons why superconductors are not yet used in high voltage grid applications. First of all in order to use superconductors in this application to their full potential the grid system will need to change from AC to DC transportation otherwise the AC loss in the cable will demand an amount of refrigeration power that will nullify the advantages. Secondly, long superconducting cables must be installed underground since the low temperature of the cable will cause materials to lose flexibility and break if used in overhead suspended power lines.

2-3 Properties of Superconductors

Normal conductors like copper have a well known electrical behaviour. For instance, the resistance of such material is almost linear with temperature. When a constant voltage is applied to a normal conductor it is the resistance of this material that will put a limit to the current. An induced current in a normal conductor would decay rapidly due to the resistive loss. A induced current in a superconducting ring will be persistent due to the absence of resistivity. There have been experiments in which a current was running for several years in a superconducting lead (Pb) ring without any measurable decay [24]. Sarangi et al. [25] showed in the beginning of this century the resistance of a superconductor at certain conditions is actually zero.

A plot of the resistance of a superconductor at constant temperature and constant magnetic field is shown in Figure 2-3. At current densities below the critical current density j_c the voltage, hence the resistance of the material, is very low. However, at increasing current densities a strong exponential increase in resistance can be seen as j_c is approached. This sudden increase in resistance is the loss of superconductivity due to high current density.

As described above a superconductor is only superconducting under certain conditions and one of the conditions is already mentioned to be the current density. Other conditions are, the temperature T and the magnetic field strength H . The plot in Figure 2-6 shows the boundary at which the transition of a superconductor takes place. The surface is called the critical surface and the corresponding current density, temperature and magnetic field strength are indicated as j_c , T_c and H_c respectively. Below the critical surface the material is in a superconducting state.

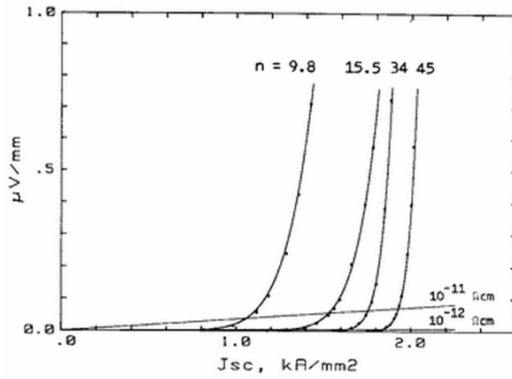


Figure 2-3 Plot of voltage versus current at $T = 4.23\text{K}$ and $B = 5\text{T}$ on NbTi filimentary conductors of large (high values of n) and small (low values of n) diameter filaments [4].

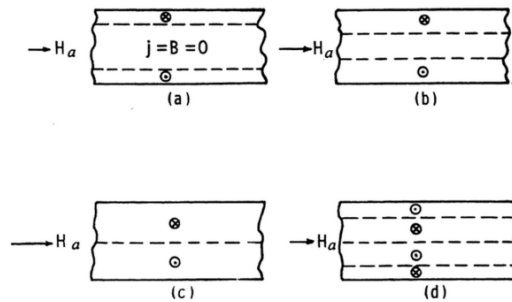


Figure 2-4 Penetration of magnetic flux into the cross-section of a superconducting slab. Induced currents are represented by the arrows going in and out of the plane of view. The field, H_a , is increasing up to full penetration (a-c) and reduces again (d) [5].

2-4 The Bean Model

The initial model introduced by Bean to describe a superconductor behaviour is based on two statements. 1) the resistance of the material is 0Ω for a current density below the critical current density, at j_c the resistance steps up towards a finite resistance and 2) j_c is independent of the magnetic field strength.

The first statement results in current penetration boundary that enter the superconductor from the surface because there is no resistance that will limit the current to rise up to j_c . Once j_c is reached at a certain location in the superconductor, the neighbouring material will start to conduct current resulting in the movement of current boundaries separating the superconductors cross-section into regions of j_c , $-j_c$ and 0 . When a temporary electric field is applied to the superconductor and removed again, the overall current will remain flowing in the same direction as the last applied electric field, similar to remanent magnetism in ferromagnetic materials. Due to no resistance the magnitude of the local current density can only take 3 values, j_c , 0 or $-j_c$ and the current density regions are separated with sharp boundaries [5]. The net current through a superconductor is changed continuously by boundary movement and therefore increasing or decreasing the size of each current density region like is shown in Figure 2-4.

At some point, the boundary movement reaches the center of the superconductor, at which the current cannot penetrate any further and the current density will start to exceed j_c . This

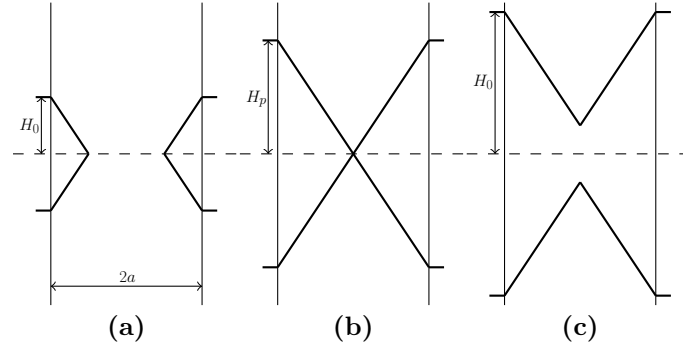


Figure 2-5 Magnetic field penetration profiles within a superconducting slab in a perpendicular field of: (a) small amplitude, (b) penetration amplitude and (c) high amplitude.

point is defined as the penetration field H_p . The current penetration is directly linked to the magnetic field penetration and therefore at H_p every part of the conductor is carrying either j_c or $-j_c$. The penetration field profile is visualised in Figure 2-5 for a slab shape superconductor in parallel field and can be calculated with

$$H_p = aj_c \quad (2-1)$$

where a is half the width of the slab. In the case of a cylindrical superconductor in a transverse field the penetration field can be calculated with

$$H_p = \frac{2}{\pi}aj_c \quad (2-2)$$

where a is the radius of a circular wire. These definitions are also used by Carr [5] and Müller [26] although it is important to state that several other well known authors in this field of study, like Wilson [6] and Ogasawara [7] use a different definition.

2-5 Extended Bean Model

The Bean model assumes that the critical current density is independent of magnetic field. However, Figure 2-6 already shows this is not the case. That is why several others, like Chen and Goldfarb [27] and Gyorgy et al. [28], extended the model with a improved definition of the critical current density, depending on the magnetic field. The Kim model is the best-known extended Bean model and has the following definition.

$$j_c = \frac{\alpha}{(B + B_e x)} \quad (2-3)$$

with α and $B_e x$ as constants at fixed temperatures [5].

2-6 Effect of Transport Current

The AC field penetration and loss in the wire is affected by a additional DC transport current. Since the transport current occupies a section of the wire, there is less current carrying

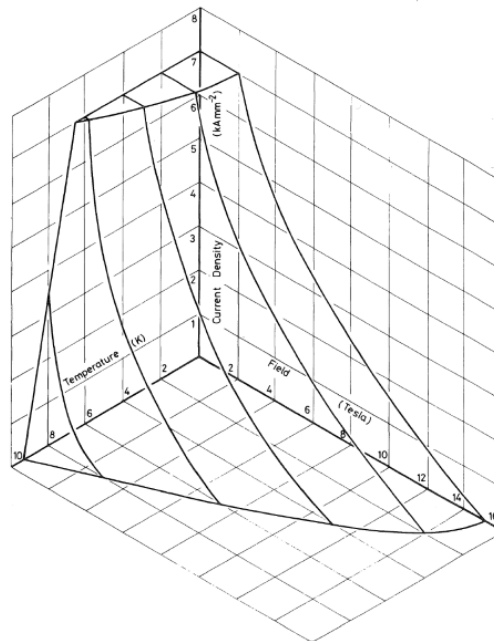


Figure 2-6 Critical current surface for an alloy of niobium-titanium [6].

'capacity' available for the AC current and field penetration. Basically the presence of a transport current reduces the penetration field and therefore has an effect on the hysteresis loss in the wire. The hysteresis loss is discussed in detail in Section 2-7 but here a short touch on this topic is started. Figure 2-7 shows the field penetration profile in the case of a slab carrying a transport current. As can be seen in the figure the penetration field is reduced due to a transport current and can be calculated with [6]

$$H_p(i) = aj_c(1 - i) \quad (2-4)$$

$$H_p(i) = \frac{2}{\pi} aj_c(1 - i) \quad (2-5)$$

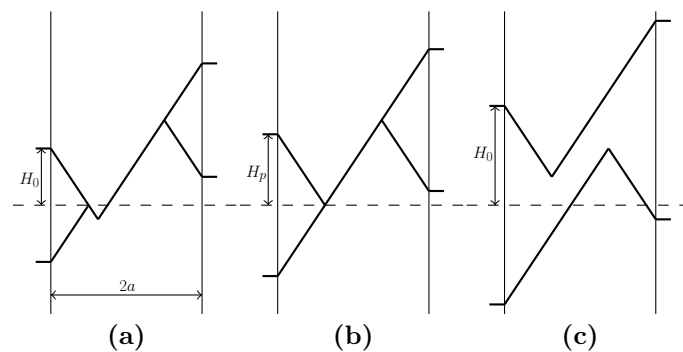


Figure 2-7 Magnetic field penetration profiles within a superconducting slab carrying a transport current and exposed to an external perpendicular AC field of: (a) small amplitude, (b) penetration amplitude and (c) high amplitude.

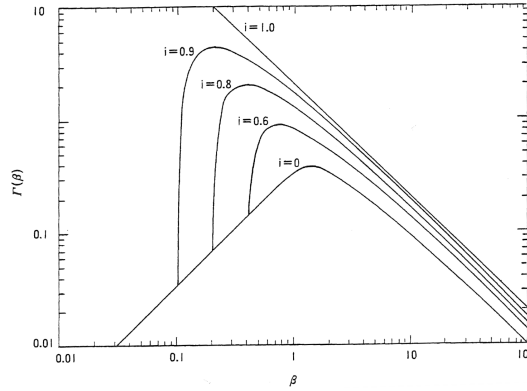


Figure 2-8 Hysteresis loss in a slab carrying a transport current in a parallel AC field. β is the ratio between the field amplitude H_0 and the penetration field H_p and Γ is the fraction of energy loss compared to the total amount of energy that is supplied via the AC field [7].

Equation 2-4 is valid for rectangular or slab shaped geometries and Equation 2-5 is valid for cylindrical geometry. i is the relative transport current defined by the transport current I_t and critical current I_c or the transport current density j_t and the critical current density j_c

$$i = \frac{I_t}{I_c} = \frac{j_t}{j_c} \quad (2-6)$$

$$\beta = \frac{B_0}{B_p} = \frac{H_0}{H_p} \quad (2-7)$$

Where β is the relative magnetic field and B_0 and H_0 the external applied magnetic flux density and magnetic field strength are. The presence of a transport current can increase the AC loss in the conductor drastically when the amplitude of the magnetic field is in the range of 0.1 to 1 H_p as can be seen in Figure 2-8. Looking at this figure it can be seen that in the case of $\beta > 1$ the hysteresis loss in the slab in the worst case doubles. Actually, the loss increases with a factor $(1 + i^2)$ [6]. But, in the case of $1 > \beta > 0.1$ the hysteresis drastically increases when a transport current is present. It should be noted the loss fraction of the total energy present in the AC field Γ reaches values above unity meaning the source of power loss is not only the AC field but the transport current as well.

2-7 AC Loss in a Superconductor

The caption of this section could thought of to be conflicting with the earlier stated property of a superconductor of lossless conductivity. However, the lossless conduction of current is only true in static situations. In the case of changing currents a superconductor is prone to loss which is referred to as AC loss.

Purely looking at the superconductor the hysteresis loss is the only mechanism causing the AC loss. However, since a superconductor wire is always built out of several non-superconducting materials for strength, stability, and insulation purposes, there are three additional types of loss occurring in the wire named eddy current loss, coupling loss and ferromagnetic loss. Figure 2-9 schematically shows the location where each type of loss occurs in the cross-section of a wire. The four types of loss are summarized below [29].

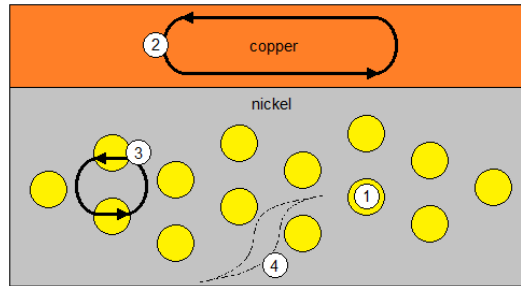


Figure 2-9 Schematic representation of types of loss occurring in a superconducting wire. Numbers in the cross-section represent: 1 hysteresis loss, 2 eddy current loss, 3 coupling loss and 4 ferromagnetic loss.

- Hysteresis loss
Caused by movement of magnetic flux lines in the superconductor.
- Eddy current loss
Caused by induced currents in the normal metal of a wire due to changing magnetic field.
- Coupling loss
Caused by cross-over currents from one filament to the other, through the normal metal regions of a wire.
- Ferromagnetic loss
Caused by hysteric behaviour of ferromagnetic non-superconducting materials of a wire.

The total AC loss in a superconductor is the summation of each loss mechanism:

$$\bar{P}_{AC} = \bar{P}_h + \bar{P}_e + \bar{P}_c + \bar{P}_f \quad (2-8)$$

Where \bar{P}_{AC} is the average AC power loss and \bar{P}_h , \bar{P}_e , \bar{P}_c and \bar{P}_f correspond to the average power loss generated by each AC loss mechanism.

Hysteresis loss in a superconductor is caused by the movement of magnetic flux into the material. This movement generates an electric field in the material, giving rise to a current. Since the current can only be 0 or j_c as is defined by the Bean model, the total shielding current can only increase by increasing penetration depth as is presented in Figure 2-4. Secondly, when the applied field is reduced, the introduced current boundary does not move back out of the material, instead a new penetration boundary of magnetic flux in the opposite direction appears at the surface of the conductor showing a hysteric irreversible process. According to Bardeen and Stephen [30], the conversion of work into heat is done in the core of a so called current vortex. At microscopic scale it is found that the magnetic field penetrates the superconductor in quantised amounts of fluxes. Each quantised amount of flux generates a current vortex shielding the superconducting parts from the penetrated field. However, the material at the core of the vortex, where the flux is passing through, loses it's superconductivity and therefore is able to carry the magnetic flux. As the flux is moving, these induced vortices move along with it. But, whenever a vortex is moving, some of it's current is passing through the non-superconducting core experiencing resistive losses, generating heat. In short, the movement of vortices through the conductor is what generates the hysteresis

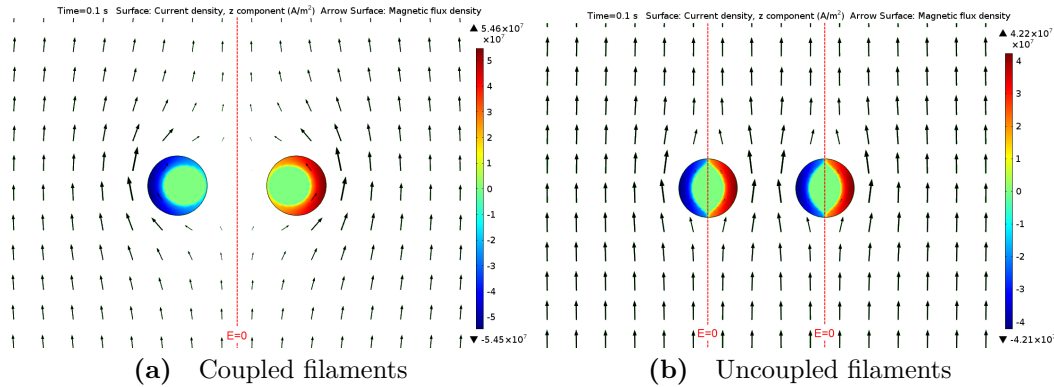


Figure 2-10 Current penetration in coupled and uncoupled filaments in a changing transverse magnetic field. The red and blue regions correspond to a current in and out of the plane. The arrows indicate the direction of the magnetic field which has reached the maximal value at the displayed time.

loss. A general way of reducing the hysteresis loss is by reducing the travelled distance of the vortices into the material by splitting the conductor into numerous microscopic filaments. A small filament diameter, results in low hysteresis loss.

Eddy current loss goes beyond superconductor applications. Electric devices as motors, generators and transformers have been dealing with this type of loss ever since they were discovered. Although, in superconductor applications they impose an additional challenge due to the very low temperatures these applications operate in as is discussed in Chapter 1. The cause of eddy current loss are the resistive losses of induced currents in the normal metal components of the wire. The general method to reduce this loss is by laminating the normal metal or by using a material with low conductivity, which both will prevent circular currents to flow perpendicular to the changing magnetic field. In superconductor wires however, these methods are usually difficult to apply since the purpose of the normal metal is mostly to stabilize and strengthen the wire which properties are both lost when using laminated and low conductivity material.

The coupling loss is discussed using Figure 2-10 that shows the difference between coupled and uncoupled filaments. In the coupled situation the filaments respond as if they are one superconducting body resulting in one filament transporting the penetrated current into the plane of the paper and the other filament carrying the same current but in the opposite direction with the line of 0 electric field outside the conductor in between the filaments. Somewhere along the length of the wire the current transfers from one filament to the other crossing the normal metal matrix generating loss. In the fully uncoupled situation each filament is not interacting with the others and therefore the current penetration occurs from both sides with the line of $E=0$ running through the superconductor eliminating the need of current to run through the matrix e.g. eliminating the corresponding loss. Similar to Grilli et al. [29] this project uses the therm coupling loss for the loss that originates in the normal metal matrix of the wire, caused by current loops from one filament to the other due to a changing magnetic field. There is a lot of similarity between coupling loss and eddy current loss since they both are circular induced currents caused by changing magnetic fields. The difference is the location where they occur as is depicted in Figure 2-9. Filament distribution largely determines the coupling loss followed by normal matrix resistivity and the contact resistance

between the superconductor and the matrix. Therefore there is no easy way in using analytical formulas that are applicable in general cases to estimate the coupling loss [31]. It is possible to estimate the asymptotic boundaries of the coupling loss by analysing the scenarios of fully coupled filaments due to low inter-filament resistivity and fully uncoupled filaments. The latter will lead to no inter-filament current and hence, no coupling loss which will also be seen from the analytical formulas in the next sections. What can be stated in general is that a short twist pitch (twist angle of filaments along the length of the wire) and high inter-filament resistivity will both result in low coupling loss [29].

Ferromagnetic materials in the wire experience hysteresis loss comparable to the superconductor which in general is referred to as hysteresis loss but since this term is already used for the hysteresis loss in the superconductor, the hysteresis loss in the ferromagnetic material is referred to as ferromagnetic loss. The presence of ferromagnetic material influences the total AC loss in the wire in two ways: the AC fields magnetise and demagnetise the material which is a hysteric process and the ferromagnetic material defects the magnetic field causing in different AC loss in the other components of the wire [29].

2-8 Analytical Calculation of AC Loss in Multifilamentary Superconductors in Transverse Field

Literature describes AC loss calculations for a broad range of situations each related to a specific application, geometry, orientation or boundary condition [5]. This is because the AC loss is a combination of several loss contributions which all depend strongly on the situation. It is of no value to discuss formulas which are not applicable in this project. Therefore this section skips the loss calculations of basic situations and goes directly into the AC loss calculation of multifilament superconducting wires in a transverse field.

As shown in Figure 1-1a the wire consists of three types of material, MgB₂ filaments, Nickel matrix in between the filaments and a single sided Copper stabilizer strip. Nickel is a ferromagnetic metal, so for this scenario all four loss mechanisms described in the previous section will need to be considered.

Since the cross-section of the wire has a complex filament shape and distribution, this will be approached by three scenarios with each having different assumptions in order to simplify the geometries and enable for analytical computation. Figure 2-11 shows an impression of the scenarios with cylindrical filaments, rectangular filaments and merged filaments. The spread in results between the three scenarios will give an indication of the boundaries where the real value will be within.

The derivation of the analytical hysteresis loss calculation for each method starts with the Maxwell equations, taken as

$$\text{curl } \mathbf{E} = -\mu_0 \dot{\mathbf{H}} \quad (2-9)$$

$$\text{curl } \mathbf{H} = \mathbf{j} \quad (2-10)$$

$$\text{div } \mathbf{E} = 0 \quad (2-11)$$

$$\text{div } \mathbf{H} = 0 \quad (2-12)$$

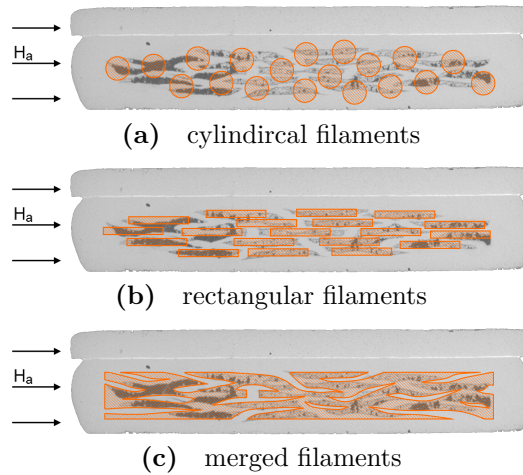


Figure 2-11 Scenarios that approximate the real wire with simplified geometries, visualised by projection of assumptions on wires cross-section.

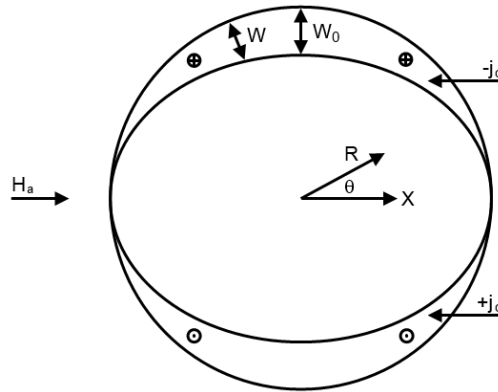


Figure 2-12 Current penetration in a cylindrical conductor filament with transverse applied field and the penetration depth w and w_0 as function of the angle θ .

assuming no polarization and constant Maxwell charge density. These assumptions hold since the material under consideration is a perfect conductor which is not dielectric. The effect of temperature and pressure on the Maxwell charge density are assumed to be negligible within the boundaries of the superconducting region of the material.

$$w = w_0 |\sin\theta| \quad (2-13)$$

Cylindrical Filaments in Slowly Changing Transverse Magnetic Field

In the first analytical approach it is assumed the filaments are cylindrical, the rate of change of the magnetic field is small enough to allow for full flux penetration, the magnetic field is acting transverse to the length of the wire, the E-J characteristic is according to the Bean approximation, the shape of the flux penetration boundary is described by Equation 2-13 and Figure 2-12 and the superconductor fill factor is low, where w is the penetration depth, w_0 is the maximal penetration depth and θ is the position angle in the cylindrical conductor. The assumption of full flux penetration implies that the field is able to reach until the center of

the wire i.e. each filament is experiencing the same field. Therefore the total hysteresis loss can be calculated by multiplying the result of one filament with the total number of filaments. Carr [5] derived an expression for the hysteresis loss under two conditions. (a) If the field amplitude is large compared to the penetration field (H_p) the average hysteresis loss per unit volume is described by [5]

$$\frac{\bar{P}_h}{V} = \lambda f \frac{16}{3\pi} j_c a \mu_0 H_0 \quad (2-14)$$

with \bar{P}_h as the average hysteresis power loss, V as the volume, λ as the superconductor fill factor, f as the frequency, a as the radius of the filaments and H_0 as the amplitude of the field. (b) If the amplitude of the field is small compared to the penetration field, the hysteresis loss can be approximated by [5]

$$\frac{\bar{P}_h}{V} \approx \lambda f \frac{256}{9\pi} \frac{\mu_0 H_0^3}{2a j_c} \quad (2-15)$$

Since both expressions of P_h are the result of assuming a slowly changing magnetic field, each filament experiences the same field and therefore calculation is independent of filament distribution.

The eddy current loss that occurs in a slab of copper has been analysed extensively since it occurs in all kinds of electrical machines. As said, the eddy current loss occur in the normal conductive components of a superconductor wire, excluding the filamentary region. In this project the wire includes a rectangular copper strip. The eddy current loss per unit volume in a solid rectangular normal-metal wire with parallel field to the width of the wire is described by [32]

$$\frac{P_e}{V} = (\pi f \mu_0 H_0 a)^2 \frac{\sigma_{nm}}{6} \quad (2-16)$$

where a is the thickness of the strip and σ_{nm} is the conductivity of the normal metal.

As described in Section 2-7 the coupling loss mechanism origins from resistive losses of an induced current in the filamentary region of the wire due to changing magnetic flux. Since the changing field is assumed to be perpendicular to the wire, the perpendicular conductivity σ_{\perp} of the matrix and superconductor needs to be determined in order to calculate the coupling loss. However this conductivity is generally not known and additionally, the matrix material is often an alloy of which the combined conductivity varies largely from the conductivity of the separate elements it is made of. For example the resistivity of a Copper-Nickel alloy at 20K is presented in Figure 2-13 showing the resistivity of pure Nickel in the left and pure Copper on the right of the plot. Almost any mixing percentage of these metals quickly boosts the resistivity of the alloy up to a factor of 1000-10,000 compared to the resistivity of Copper or Nickel.

In order to analytically approach the perpendicular conductivity of filament-matrix region, the literature introduces the "anisotropic continuum" model that in the calculations replaces the matrix and filaments by a continuum with a isotropic conductivity parameter [33]. At the heart of this model lays the definition of the perpendicular conductivity based on two distinct situations. Either the filament to filament resistivity is assumed to be large, for instance due to an insulating alloy layer surrounding the filaments or either the filament to

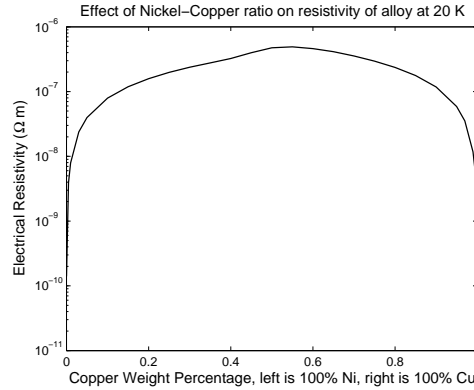


Figure 2-13 Resistivity digram of Cu-Ni alloy for varying compositions at 20K [8]

filament resistivity is assumed to be low, for instance due to high matrix conductivity or good filament to matrix contact. The first case is generally applicable on wires that use low conductivity matrix material like alloys, the second case is a better approximation in the case of high conductivity matrix material like a pure copper. Both situations are described, to good approximation, by

$$\sigma_{\perp} = \sigma_m \frac{(1 + \lambda)}{1 - \lambda} \quad (2-17)$$

$$\sigma_{\perp} = \sigma_m \frac{(1 - \lambda)}{1 + \lambda} \quad (2-18)$$

where in Equation 2-17 the filament to matrix conductivity is small resulting in currents to prefer to run through the superconductor material. The assumption results in a relatively higher conductivity compared to the conductivity of the matrix σ_m . Equation 2-18 approximates a high filament to matrix resistivity resulting in currents that tend to avoid the superconducting regions. Experiments have shown the first expression is usually a good approximation at high conductive matrix material. Naturally as $\lambda \rightarrow 1$ the results are least accurate [34].

The average coupling loss per unit volume generated in a circular multifilamentary wire in a slowly changing magnetic field is [5]

$$\frac{\overline{P}_c}{V} = (2\pi f)^2 \frac{\sigma_{\perp} (\mu_0 H_0)^2}{2} \left[\left(\frac{L}{2\pi} \right)^2 + \frac{a_0^2}{4} \right] \quad (2-19)$$

were f and H_0 are the frequency and amplitude of the field, L is the filament twist pitch and a_0 is the radius of the filamentary region of the wire [5] [32]. The right term in the squared brackets represents the loss in the wire as if it was made out of isotropic matrix material i.e. no superconducting material. The left term represents the change in coupling loss due to the presence of the superconductor filaments.

Equation 2-19 is valid for a circular geometry of the wire. However, in this scenario the cross-section is assumed to be rectangular. It is very complex to derive an analytical expression for the coupling loss in a rectangular twisted multifilamentary wire since the path of the filaments along the length of the wire cannot simply be described by assuming a spiralling

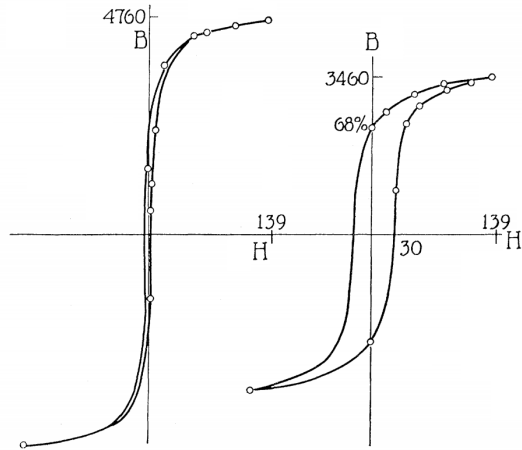


Figure 2-14 B-H curves of two samples of nickel films showing hysteric behaviour. The left curve is a well-annealed nickel wire and the right curve is an unannealed sample of the same wire [9].

trajectory. In order to estimate the coupling loss with the use of Equation 2-19 the surface area of the rectangular filamentary region is used to derive the radius of a circular wire with the same surface area. Since the field is assumed to change slowly enough to fully penetrate to the center of the wire this assumption will not have an additional increase in the error. In the case of slowly changing low amplitude AC fields the hysteresis loss is expected to be the dominant loss [35]. According to Oomen et al. [36] the eddy current loss in multifilamentary superconductors is only significant at high field amplitudes, based on experimental results where the amplitude of the field was varied from 0.001-0.7T at a frequency of 50Hz.

Nickel is a ferromagnetic material which, placed in a changing magnetic field will generate heat referred to as the ferromagnetic loss. The cause of the ferromagnetic loss is the magnetization of the material which is a hysteric process as shown in Figure 2-14. Literature describing this loss refer to it as hysteresis loss which is correct. However since this project also treats the hysteresis loss in a superconductor which is treated entirely different, the nomenclature is slightly different. The ferromagnetic loss is determined by the surface area within the B-H curves and therefore it can already be seen the loss per cycle is independent of frequency. Translating this into analytical equations the result is

$$E_f = V_{fer} \oint H dB \quad (2-20)$$

$$\frac{P_f}{V} = \lambda_{fer} f \oint H dB \quad (2-21)$$

with λ_{fer} as the fill factor of the ferromagnetic material in the cross-section of the wire. The shape of the B-H curve is non-linear and multivalued which cannot be described by a simple mathematical expression. Even materials with the same chemical composition can show very different B-H curves due to a different treatment as is demonstrated in Figure 2-14. Therefore it is difficult to directly derive an analytical expression for the ferromagnetic loss. According to Steinmetz, based on a large number of experiments, the B-H relation of bulk material can be approximated by [10]

$$P_f = K_h B_{max}^n f \quad (2-22)$$

where K_h is a constant depending on volume and type of material that can be empirically determined and n is the exponent that varies from 1.5 to 2.5. Transforming Equation 2-22 to the non-bulk material of a superconducting wire with ferromagnetic components results in

$$\frac{P_f}{V} = \lambda_{fer} f K_h B_{max}^n \quad (2-23)$$

Rectangular Filaments in Slowly Changing Parallel Magnetic Field

The filament geometry could be assumed to be rectangular instead of cylindrical. A rectangular superconductor in a parallel magnetic field generally generates less losses compared to the same geometry in a perpendicular applied field. The assumed situation in this scenario is a strip shaped filament. The cross-section of a filament is rectangular with width w_r and thickness $2a$. The AC field is acting parallel to the width, and perpendicular to the length of the strip and $H_0 < H_p$. The hysteresis loss per meter length in a filament, using Bean critical state model is described by [26]

$$P_h = \frac{2\mu_0}{3\pi} \omega w_r a [3H_0 H_p - 2H_p^2] \quad (2-24)$$

$$P_h = \frac{2\mu_0}{3\pi} \omega w_r a \frac{H_0^3}{H_p} \quad (2-25)$$

Where Equation 2-24 is valid for $H_0 > H_p$ and Equation 2-25 is valid for $H_0 \leq H_p$ with H_p defined by Equation 2-1 and ω is the rotational speed. Assuming the field acting on each filament is the same, the average hysteresis loss per unit volume of the wire is

$$\frac{\overline{P}_h}{V} = \lambda f \frac{4}{3} \mu_0 [3H_0 H_p - 2H_p^2] \quad (2-26)$$

$$\frac{\overline{P}_h}{V} = \lambda f \frac{4}{3} \mu_0 \frac{H_0^3}{H_p} \quad (2-27)$$

Where Equation 2-26 is valid for $H_0 > H_p$ and Equation 2-27 is valid for $H_0 \leq H_p$. This scenario assumes the same geometry for the normal metal components of the wire, hence the eddy current and ferromagnetic loss can be calculated using Equation 2-16 and Equation 2-23.

The formulation of the coupling loss in Equation 2-19 is a general expression for the loss per volume of conductive material independent of geometry. The geometry dependence is caught in the formulation of the transverse conductivity σ_{\perp} of Equation 2-17 although according to Carr [5] the expression is relatively independent of geometry when considering simple filament shapes. Since one of the assumptions is a low superconductor fill-factor and a rectangle is considered to be a simple geometry, Equation 2-18 in combination with Equation 2-19 is applicable in this scenario for approximating the coupling loss.

Merged Filaments in Rectangular Shape

In this analytical approximation, the filaments are assumed to be completely merged together. The geometry is acting as a fully coupled conductor in the shape of a rectangular strip mixed

with regions of matrix material as shown in Figure 2-11c. The difference with the other scenarios is the assumed thickness of the superconductor. In this scenario there is no need to consider the number of filaments since they are assumed to be merged together acting as one conductor.

The superconductor geometry is a rectangle and therefore the hysteresis loss per unit volume can be calculated using Equation 2-26 and 2-27 where a is half the thickness of the coupled superconductor region. For correct comparison, λ cannot be derived from the width and height of the superconductor area ($A_{sup} \neq 4ab$) since that would unintentionally include the normal metal matrix.

Assuming the filaments to be coupled results in a current penetration as shown in Figure 2-10a although the picture shows separated filaments which is currently not the case. This does not mean the coupling loss is zero or maximal since the superconductor region in the wire's cross-section still contains the same amount of normal metal matrix, exhibiting coupling loss. Nickel as matrix material leads to the assumption the coupling-currents (basically eddy-currents in the matrix) to avoid running through the superconductor material (Equation 2-18). In this scenario there is no reason to abandon this assumption since the matrix material still is a good conductor and the superconductor fill factor λ has not changed. Therefore Equation 2-19 can be used to calculate the coupling loss.

Eddy current and ferromagnetic loss in this scenario have the same assumptions and conditions and therefore can be calculated using Equation 2-16 and 2-23.

2-9 Numerical Modeling of Superconductors

The AC loss of a superconductor can also be analysed with numerical modeling. The specific type of numerical modeling technique in this project is the Finite Element Method (FEM). In this mathematical method the computational capacity of computers is used to solve partial differential equations which cannot be solved analytically. This is done by dividing the geometry of investigation, in this case a superconducting generator, into small finite elements which is called meshing. Figure 2-15 shows an example of a triangular mesh of a generator dividing the 2d geometry into 54670 domains. The interaction between each element is described by differential equations of the physics involved. For instance, when solving a electro-magnetic problem the Maxwell equations, in differential form, are used. Together with the supplied boundary conditions the method attempts to minimize an error function leading to a stable solution which approaches reality.

One of the possibilities for FEM calculations is to create your own script in a mathematical program. However, there are also software packages available for FEM modeling which have a user friendly interface and contain all the differential equations required for basic physics and also include a library with often used materials. The software used in this project is Comsol Multiphysics®.

Superconductors are not included in the material library of Comsol thus this material needs to be defined manually. One of the challenging aspects of modeling superconductors is the relation between current density and electric field. The resistance or conductivity of a normal conductor is independent of current density and can therefore be described by Ohm's law. In a superconductor, Ohm's law is still valid, although the resistance of the conductor needs to

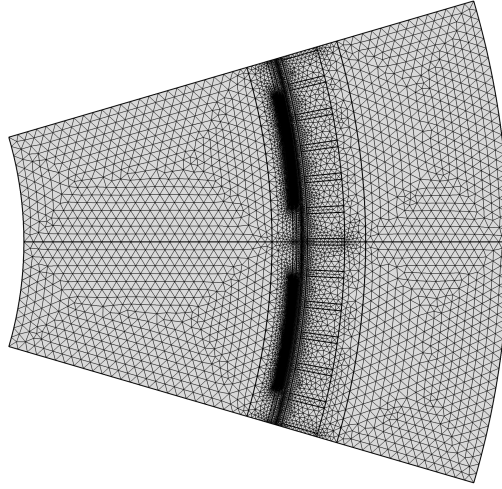


Figure 2-15 2d mesh of a pole pair with a very fine mesh near the air-gap.

be defined as a function of the current density. The basic 'Magnetic Field' physics designed by Comsol is not able to solve this because a circular dependence occurs in solving the current density. However, it is possible to use the magnetic field as dependant variable and solve the current density with Faraday's law given in equation 2-9. This approach is based on a suggestion by Brambilla [37].

Measurements of the resistance of a superconductor as function of the current density can be fitted to a power law expression as is shown in Figure 2-3. The n -power law [4] can be used to define the E-J characteristics of a superconductor as

$$\mathbf{E}(\mathbf{J}) = E_0 \left(\frac{|\mathbf{J}| - J_c}{J_c} \right)^\gamma \frac{|\mathbf{J}|}{\mathbf{J}} \quad (2-28)$$

where E_0 and γ are constants used for fitting the E(J) curve to the measurements.

2-10 Loss Calculations in the Frequency Domain

The hysteresis, coupling and ferromagnetic loss calculations are independent of frequency. The resulting power-loss of these cyclic losses however are depending on frequency. The eddy-current power loss is even stringer depending on the frequency since in this equation the frequency is squared. One of the problems with analytical calculations is that the magnetic field in most cases cannot be described by a single frequency and amplitude but is usually a non sinusoidal shaped periodic signal containing multiple frequencies.

It is possible to take a complex shaped periodic signal and separate it into a row of sine's and cosines and amplitudes by using the Fourier transformation. Then, each frequency component of the signal represents a small part of the total and when the sum of all sine's and cosines is taken, the initial signal is the result. The result of a Fourier transformation on a time dependent signal will result in a spectrum which represents the amplitude of each frequency that is present in the time dependent signal.

For instance, when calculating the resistive loss in a multi-frequency problem it is correct to calculate the loss of each frequency component in the frequency domain, and add them to get the total loss. This is correct because the resistive loss is linear with the instantaneous voltage and current. Unfortunately, this method is not valid for hysteresis, eddy-current, and coupling loss calculations since these are not linear with the amplitude of the magnetic field as can be seen in the given equations for each loss component.

This shows the analytical calculation fails in multi-frequency problems and the need for assumptions arises. For instance, if a single frequency is clearly larger in amplitude, i.e. dominant compared to the other frequencies, then the smaller frequencies can usually be neglected since the amplitude is cubed in the hysteresis loss. Assumptions like these are discussed further in Chapter 3.

2-11 Time and Space Harmonics

AC loss in electrical machines occur in all components of the machine and are present in any type of machine. Especially in a superconducting generator, the analysis of these losses is of high importance. When only considering the superconducting field windings of a synchronous machine, the AC loss is caused by AC currents in the field winding and AC magnetic fields acting on the field winding. In general these AC sources are categorised in two groups, time harmonics and space harmonics.

Time harmonics are caused by 1) AC signals superimposed on the DC current of the field winding, for instance caused by the field winding power electronics and 2) non-sinusoidal currents in the armature windings containing harmonic distortions caused by the load. Especially in wind turbine applications which use a full back-to-back converter the armature winding could carry a current that is far from sinusoidal since these converters operate at high switching frequencies. Time harmonics are called time harmonics because they are caused by sources that are changing in time or changing non-sinusoidally in time.

Loss in the field windings due to high frequency time harmonics can be eliminated by installing a shielding conductive layer around the winding, acting as an Electro Magnetic (EM) shield. The frequency of the time harmonic and the thickness of the shield determine the amount of EM attenuation that occurs in the shield. The skin depth of the current induced in a highly conductive shield is defined as the depth below the surface at which the current density is attenuated to e^{-1} . The skin depth δ can be calculated with

$$\delta = \sqrt{\frac{\rho}{\pi f \mu_r \mu_0}} \quad (2-29)$$

where ρ is the resistivity, f the frequency and μ_r is the relative magnetic permeability of the shield material. A rule of thumb is to use 4 times the skin depth to absorb the whole EM of that frequency. Theoretically it is not possible to absorb all EM but after 4 times the skin depth only $e^{-4} \approx 1.83\%$ of the surface current is remaining.

Space harmonics are caused by non-sinusoidal winding distribution and non constant reluctance in the tangential direction along the armature of an electrical machine. This will cause a non-sinusoidal field distribution which will generate AC fields in the rotor e.g. AC loss. In the ideal situation, the armature windings of a synchronous machine produce a perfect sinusoidal

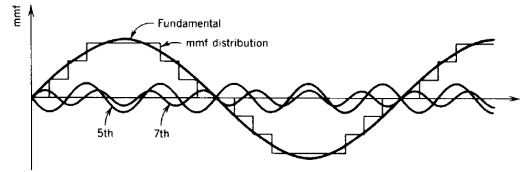


Figure 2-16 The MMF in the airgap of a typical 3-phase electrical machine [10].

field distribution but due to building restrictions like material strength, magnetic reluctance and limited space, compromises have to be made regarding the winding distribution. Additionally it is usually required to use iron teeth in between the armature windings in order to reduce the reluctance. When the field windings rotate along the armature the harmonic content of the magnetic field distribution causes AC loss in the windings. Space harmonics are called space harmonics because they origin from non-ideal winding distributions and varying reluctance and only have effect at moving objects.

In a three phase machine, the harmonic distortion of the magnetic field is coming from only a few harmonic orders. The family of space harmonics is described by

$$h = 6m \pm 1 \quad (2-30)$$

where m is a positive integer. Figure 2-16 shows the fundamental frequency and the most common 5th and 7th harmonic. The reference frame of these harmonics is the armature winding and in this frame the $h = 6m + 1$ harmonic waves run in the same direction as the rotor rotation. The $h = 6m - 1$ harmonics run in to opposite direction. However, when the reference frame of the field winding is used, which can be thought of as the point of view seen from the rotor which sees the armature windings passing by in the direction of motion, then the harmonic content can be described by

$$h = 6m \quad (2-31)$$

since the rotation of one pole pair, which is exactly one cycle of the fundamental frequency, the field winding passes 6 armature windings and teeth which are responsible for the space harmonics. This is valid in the case of single slot windings. If the armature windings are distributed over several slots, the harmonic content will shift towards higher orders of the fundamental frequencies but will still be multiples of 6 as described in Equation 2-31.

Chapter 3

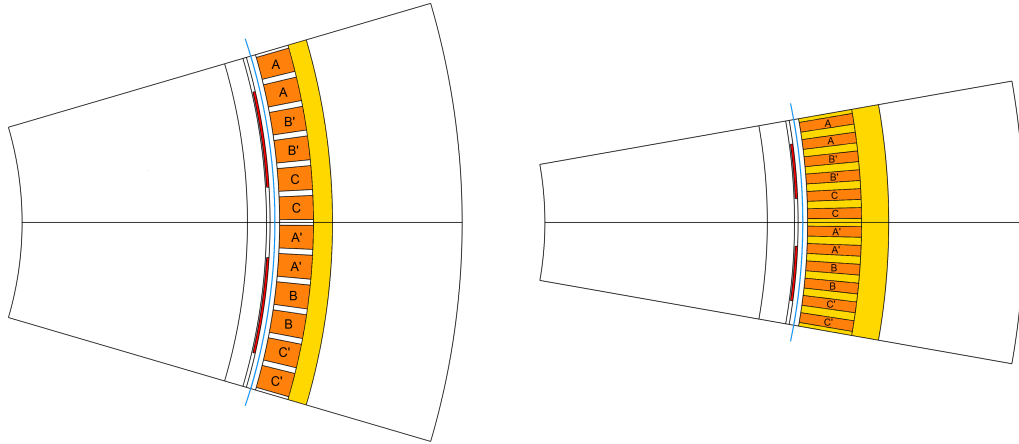
Research Methods

This chapter describes the research methods of the analytical and numerical analysis. The aim is to describe the methodology in a short and condensed manner, but extensive enough for others to copy, yielding the same results. Throughout this chapter the theory which was discussed in Chapter 2, will be applied on two designs of superconducting generators. First the analytical method will be treated, followed by the numerical method. At the end of this chapter, a partial validation of the analytical method is given by comparing experimental results with the results of the analytical calculations of the same setup.

3-1 General Approach

Two generator designs are analysed in this project, a Non Magnetic Teeth (NMT) machine and an Iron Teeth (IT). These designs are optimised for lowest costs of active material and are supplied by Dong Liu [38]. Figure 3-1a and 3-1b show the cross-section of a single pole pair of both machines and point out regions of: normal conductor material (armature winding), superconducting material (field winding), iron, and non-magnetic material. In the analysis of the time harmonics, a 10mm thick copper Electro Magnetic (EM) shield which will be applied to the rotor is assumed to absorb all high frequency time harmonics. In the analytical analysis of the space harmonics and in the numerical modeling, this shield is not considered which will lead to a worst-case result since the shield will absorb some of the space harmonics. Table 3-1 gives the exact parameters of both generator designs that are of influence on the magnetic field and AC loss in the superconducting field winding. For each generator design, all wire geometries, discussed in section 2-8, are analysed. These three scenarios consist of cylindrical filaments, rectangular filaments and merged filaments.

The general approach is to analyse the AC loss in the field windings by analytical calculations. The analytical calculations are partly validated in two ways. One is a literature validation based on the same AC loss calculations and the second is by applying the methodology of this project on an experimental set-up and compare the outcome with the experimental results [39].



(a) NMT machine

(b) IT machine

Figure 3-1 Cross-section of one pole pair of the NMT and IT generator designs with the iron (yellow), armature winding (orange), field winding (red) and center of air gap (blue), representing the boundary between rotating and static reference frames. White indicates non ferromagnetic material.

Table 3-1 Generator design parameters

Parameter	Symbol	Unit	AT generator	IT generator
nr of pole pairs	p	-	11	18
rotor outer radius	r_{r2}	m	2.460	2.460
stator inner radius	r_{s1}	m	2.500	2.500
field winding inner radius	r_{f1}	m	2.450	2.450
field winding thickness	d_f	m	0.010	0.010
armature winding inner radius	r_{a1}	m	2.500	2.500
armature winding thickness	d_a	m	0.142	0.226
yoke inner radius	r_y	m	2.642	2.726
yoke thickness	d_y	m	0.180	0.114
EM shield (not modelled)	d_{EM}	m	0.010	0.010
field winding sector angle	α_s	$^\circ$	104/p	96/p
slots per armature winding	-	-	2	2
armature slot/teeth width ratio	τ	-	0.2	0.43

3-2 Analytical Methodology

All loss equations in Chapter 2 require the amplitude and frequency of magnetic field as input. When designing a generator the space harmonics and time harmonics, causing the AC loss, are generally not known. One possibility for the space harmonics is to assume a dominant frequency and derive the amplitude by assuming a square shaped field distribution from concentrated windings. Inevitably this method will result in a large over-estimation of the field strength and since the hysteresis loss in a superconducting wire is proportional to H_0^3 ($\beta < 1$) and the coupling and eddy current loss are proportional to H_0^2 , the over-estimation in the loss calculations will be even larger.

A more accurate method in determining the space harmonics is numerical modeling of the magnetic field with Finite Element Method (FEM). Here, the magnetic field distribution is calculated based on the design of the machine. The time harmonics are determined using an analytical model of the electrical system. Once the space and time harmonics are known, the analytical AC loss calculation can be applied to get the loss throughout the field winding. This procedure is not completely analytical due to the numerical computation that is used in determining the magnetic field distribution. However, the loss calculation are solved analytically and therefore this method is referred to as the analytical methodology. The flow chart of Figure 3-2 shows each step of the process which are described in the following subsections in this Section.

Magnetic Field Modeling

The magnetic field distribution is numerically modelled in which the whole machine is assumed to have the magnetic reluctance of air with exception of the iron yoke and teeth as shown in Figure 3-1. The armature magnetic field is produced by applying a sinusoidal current density to each armature winding with a frequency of 1.199Hz in the NMT machine and 1.926Hz in the IT machine. The rotor field is created by allocating a constant current density to the field winding assuming a uniform distributed current density. To obtain good resolution of the magnetic field inside the field winding the result is radially sampled in 10 steps along the thickness of the winding and tangentially sampled in 900 steps (Figure 3-3). In order to analyse the space-harmonics of the machine, the magnetic field distribution is computed over time for the duration of the rotation of one pole with a resolution of 200 time steps. The time dependent magnetic field distribution is computed over a range of generator torque from 0 to maximal torque in 11 steps. The torque is controlled by changing the phase of the armature field from 0° to $\pm 90^\circ$ with respect to the rotor field and is therefore referred to as the field angle. The AC loss at varying torque is symmetrical around the no-load point (zero torque) in the case of symmetrical field pole and armature teeth design. Therefore it is sufficient to consider the one-sided torque range. In total, this method results in $10 \times 900 \times 200 \times 11 = 19.8 \times 10^6$ data points per analysed machine design.

Amplitude and Frequency Calculation

Once the field distribution is solved this data is transformed from time to frequency domain using Fourier transformation. In the frequency domain the data consists of multiple frequencies and amplitudes but, as pointed out in Section 2-10 the loss equations are only valid

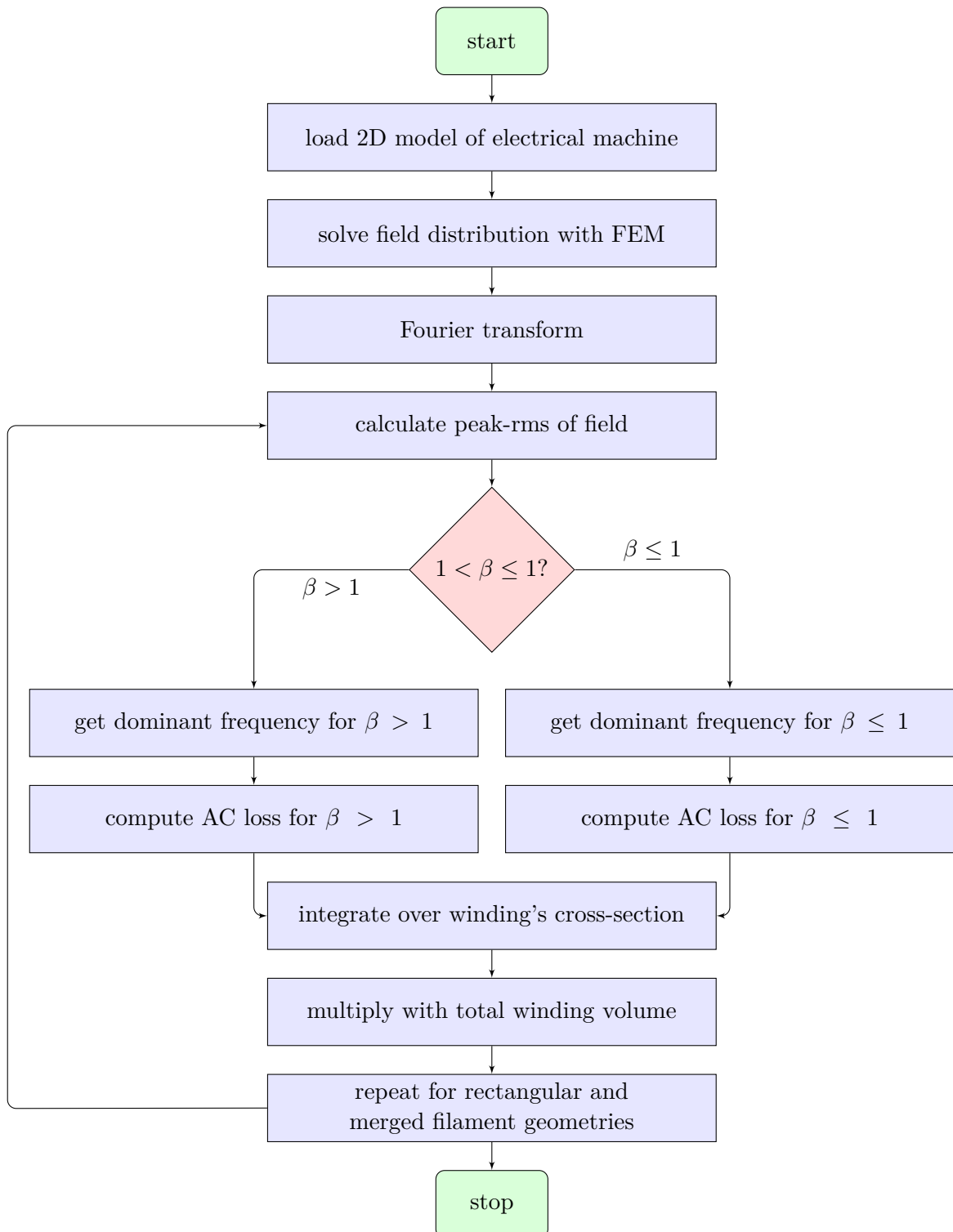


Figure 3-2 Flowchart of analytical methodology

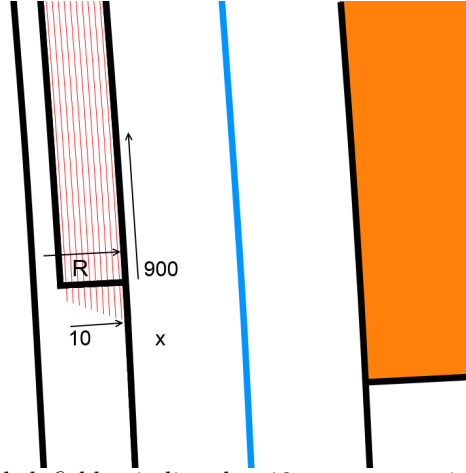


Figure 3-3 Radially sampled field winding by 10 curves ranging from $R= 2.505m$ till $R=2.595m$.

for a single frequency and amplitude. Therefore a method is derived to determine a single dominant frequency and amplitude.

The green line in Figure 3-4a, 3-4b and 3-4c show the flux density variation in time of one node in the field winding. The amplitude of the flux density is not constant in time but the analytical calculations assume a constant amplitude. So, what method suits best in determining the amplitude of the signal? Several methods can be thought of, for instance: (a) the use the maximum and minimum value of the field which results in a over estimation of the AC loss or (b) the use of the Fourier coefficient of the dominant frequency which results in a under-estimation of the AC loss. In this research the peak root-mean-square (peak-rms) value is used to determine the amplitude of the time dependent field, as is illustrated by the blue line in the figures. The peak-rms value of the field can be calculated with

$$H_{peak-rms} = \sqrt{2} \sqrt{\frac{1}{F_s t_p} \sum_{t=0}^{t_p} H(t)^2} \quad (3-1)$$

where F_s is the sample frequency of the time dependent data t_p is the elapsed time after the rotation of one pole and t is the time in seconds.

The dominant frequency is defined as the frequency that contributes the most to the AC loss. It is incorrect to simply use the frequency with the largest amplitude since the AC loss is not linear depending on the amplitude and also depending on frequency. The correct approach is to select the dominant frequency based on the AC loss contribution which can be done with an equation that selects the dominant frequency. This equation would need to 'switch' from one harmonic frequency to the other once the AC loss contribution in both frequencies is equal. Such equation, for the condition of $\beta \leq 1$, is derived below where the derivation starts with Equation 2-8.

$$\bar{P}_{h6} + \bar{P}_{c6} + \bar{P}_{e6} = \bar{P}_{h12} + \bar{P}_{c12} + \bar{P}_{e12} \quad (3-2)$$

$$C_h f_6 \hat{H}_6^3 + C_c f_6^2 \hat{H}_6^2 + C_e f_6^2 \hat{H}_6^2 = C_h f_{12} \hat{H}_{12}^3 + C_c f_{12}^2 \hat{H}_{12}^2 + C_e f_{12}^2 \hat{H}_{12}^2 \quad (3-3)$$

$$C_h f_6 \hat{H}_6^3 + f_6^2 \hat{H}_6^2 (C_c + C_e) = C_h f_{12} \hat{H}_{12}^3 + f_{12}^2 \hat{H}_{12}^2 (C_c + C_e) \quad (3-4)$$

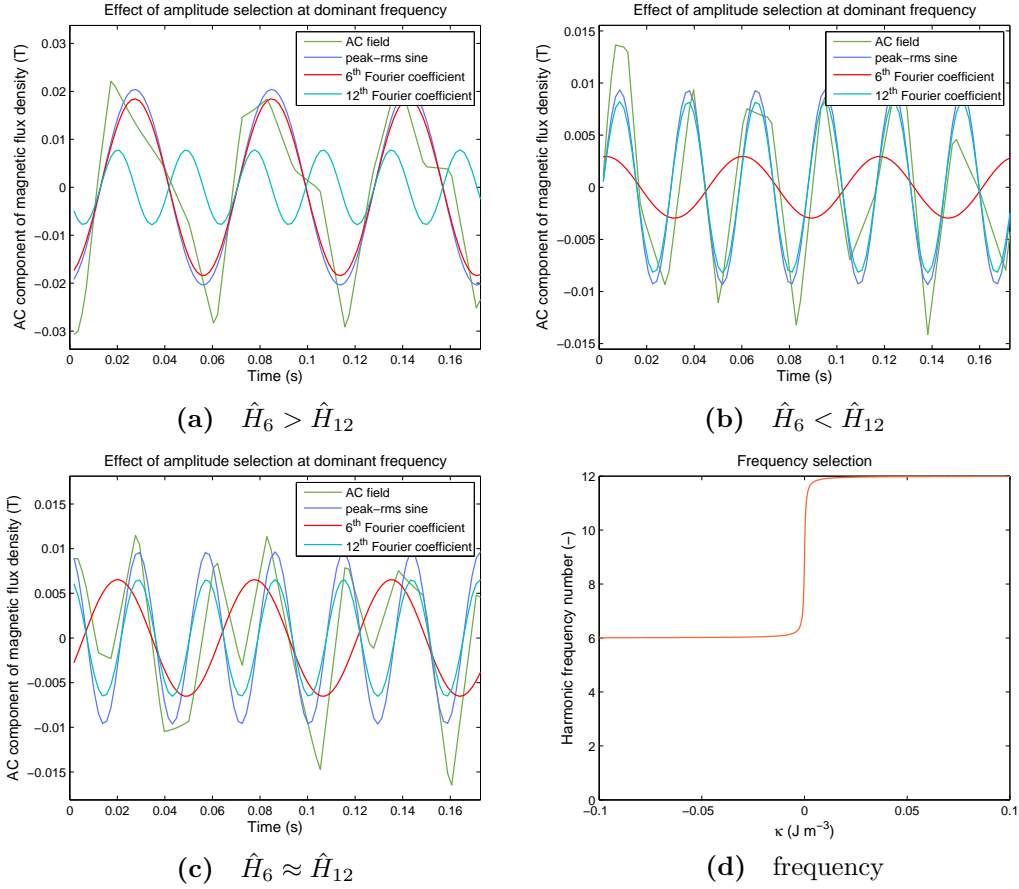


Figure 3-4 Result of selection of dominant frequency by equation

Where the number in the subscript of the Equations 3-2 till 3-4 refers to the harmonic frequency, C_h , C_c and C_e represent the non-variable or constant factors of the AC loss components, f is the frequency and \hat{H} the corresponding amplitude. Since $f_{12} = 2f_6$ and $C_e \ll C_c$ for long filament twist pitch, Equation 3-4 can be simplified to

$$\frac{C_c}{C_h} f_6 (4\hat{H}_{12}^2 - \hat{H}_6^2) + 2\hat{H}_{12}^3 - \hat{H}_6^3 = \kappa \quad (3-5)$$

The variable κ shows which harmonic frequency is dominant. If the 12th harmonic frequency is dominant then the value of κ is positive and if the 6th harmonic frequency is dominant, κ is negative. When $\beta > 1$ the AC loss equations are different and therefore the expression for κ is also different. The derivation follows the same procedure, starting with Equation 3-2

$$\bar{P}_{h6} + \bar{P}_{c6} + \bar{P}_{e6} = \bar{P}_{h12} + \bar{P}_{c12} + \bar{P}_{e12} \quad (3-6)$$

$$C_h f_6 \hat{H}_6 + C_c f_6^2 \hat{H}_6^2 + C_e f_6^2 \hat{H}_6^2 = C_h f_{12} \hat{H}_{12} + C_c f_{12}^2 \hat{H}_{12}^2 + C_e f_{12}^2 \hat{H}_{12}^2 \quad (3-7)$$

$$C_h f_6 \hat{H}_6 + f_6^2 \hat{H}_6^2 (C_c + C_e) = C_h f_{12} \hat{H}_{12} + f_{12}^2 \hat{H}_{12}^2 (C_c + C_e) \quad (3-8)$$

$$\frac{C_c}{C_h} f_6 (4\hat{H}_{12}^2 - \hat{H}_6^2) + 2\hat{H}_{12}^3 - \hat{H}_6^3 = \kappa \quad (3-9)$$

Equation 3-5 and 3-9 describe κ for the case of $\beta \leq 1$ and $\beta > 1$ respectively. Each κ value

can be translated into a dominant frequency with

$$f = f_6 \left[\frac{3}{2} + \frac{1}{\pi} \arctan(2 \times 10^3 \kappa) \right] \quad (3-10)$$

where f is the resulting frequency used in the loss calculations. The factor inside the arctan is added to create a smooth but short transition interval from one frequency to the other and is empirically found. Figure 3-4d shows the result of Equation 3-10 as function of κ which is continues for all real values of κ . The dominant frequency is evaluated at every position in the field winding and at all field angles.

Relative Penetration Field and AC Loss Calculation

To calculate the dominant frequency and the total AC loss, β needs to be known (see Figure 3-2). Since, only a selection of the equations given in Section 2-7 are applicable on this project a short summary of the applied equations in each scenario is added below.

- Penetration field
 - rectangular geometry - Eq. 2-4
 - cylindrical geometry - Eq. 2-5
 - relative penetration field, β - Eq. 2-7
- Hysteresis loss
 - $\beta > 1$
 - cylindrical filaments - Eq. 2-14
 - rectangular and merged filaments - Eq. 2-26
 - $\beta \leq 1$
 - cylindrical filaments - Eq. 2-15
 - rectangular and merged filaments - Eq. 2-27
- Eddy current loss
 - all scenarios - Eq. 2-16
- Coupling loss
 - all scenarios - Eq. 2-19

Volume Averaging

The final steps in the analytical methodology consist of integrating the loss over the cross-section of the winding and multiplying with the total volume of winding material in the machine. In the beginning of the analytical calculation, the cross-section of the field winding is divided into 9000 nodes of which the field is extracted. At the end of the methodology, the result of each node is combined into a total result by integration over the field windings cross section.

Since all loss equations are expressed in the form of power per unit volume, the result is multiplied with the total volume of the field winding to get the total AC loss.

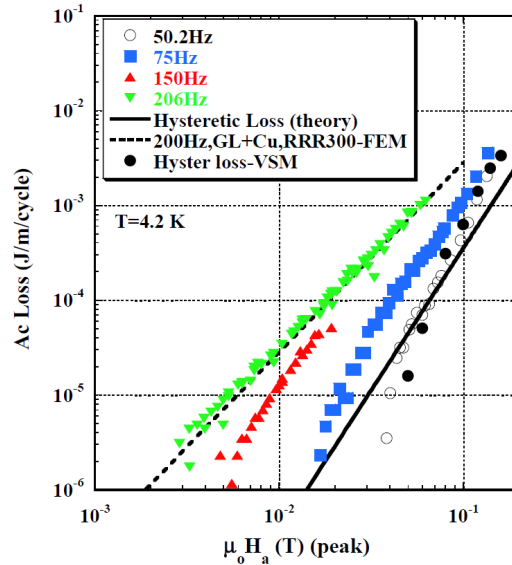


Figure 3-5 Theoretical and experimental AC loss of NbCu7-ODS wire. The symbols are measurements and the lines are calculated [11]

3-3 Experimental Validation of Analytical Methodology

Described methodology is based on theory and assumptions. The theory is partly validated and together with the assumptions the analytical calculations are invalidated. To show the accuracy of the theory and methodology two validations are described in this section. The first validation is from literature and the second validation is done in this research based on experimental results.

Majoros et al. [11] published a validation of a cylindrical multifilament MgB2 wire with copper stabilizer. The wire is exposed to a small external field ($\beta < 1$) ranging from 0.002T to 0.2T with a frequency range from 50Hz to 200Hz. Particularly the frequency range of this experiment is of interest because it is expected to be comparable to the frequency range of this research. More details on the validation can be found in [11]. Figure 3-5 shows the measured AC loss of the wire and the theoretical calculated hysteresis loss. At 50Hz the hysteresis loss calculation is, according to the authors, "quite satisfactory" matching with the measurements. As the frequency is higher the eddy current loss contribution is more relevant which points out a single hysteresis loss calculation is not sufficient.

Next to the literature validation of Majoros, a second validation is done in this research, covering a different frequency and amplitude range. Experimental results, supplied by Marc Dhallé (University of Twente) are used for this validation. The document, containing the experimental results is not published and therefore it is added in Appendix A. In this experiment an 1.2m sample of MgB2 multifilamentary wire exposed to a changing perpendicular field while the magnetization of the sample is measured. Figure 3-6a shows the cross section of the wire and Figure 3-6b shows the magnetization loop at oscillating flux density from 1T to 3T at a frequency of 2mHz. In comparison to the experiment of Majoros et al. this experiment considers much higher field strength at much lower frequencies. The amplitude range causes beta to exceed unity ($\beta > 1$) in contrast to the validation of Majoros et al.

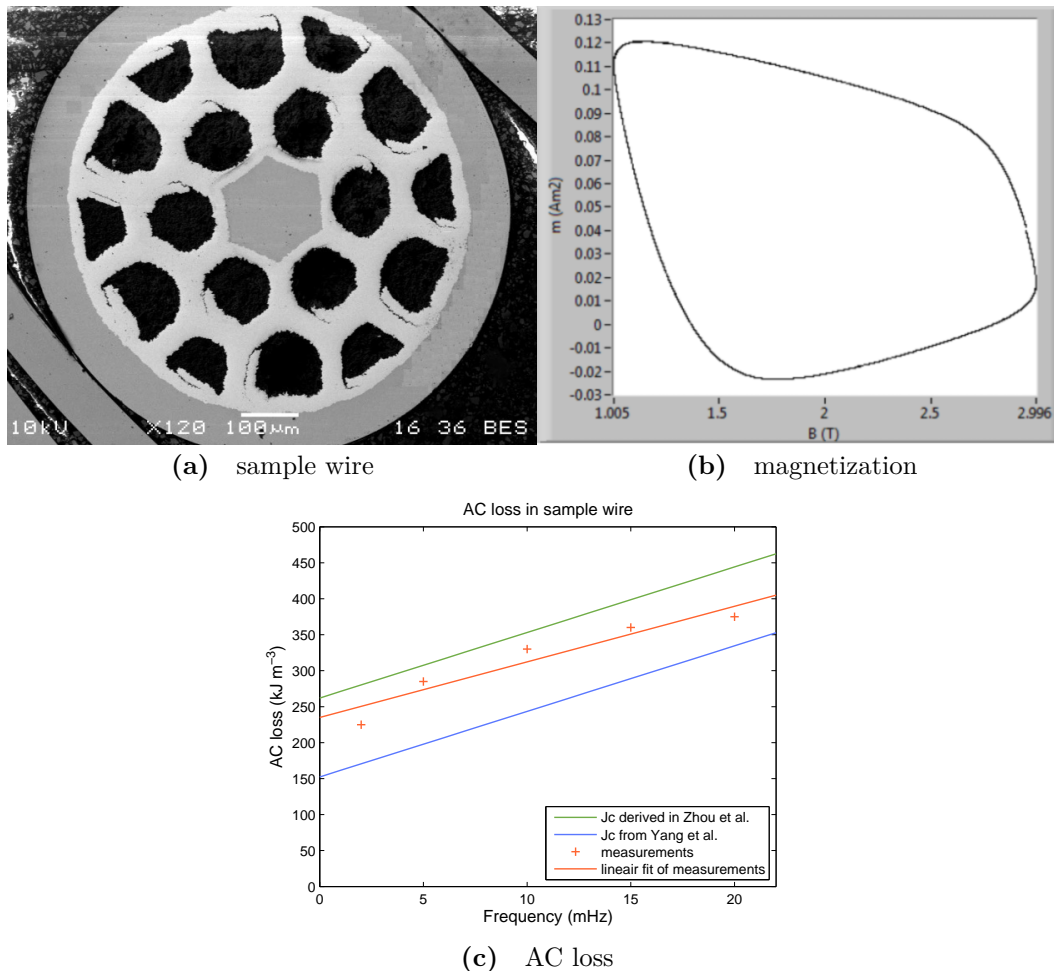


Figure 3-6 Cross section of the multifilamentary wire used in the experiment, the magnetization loop measured at 4.2K when flux density is changed between 1 and 3T with a frequency of 2mHz and the theoretical and experimental loss per frequency of MgB2 wire 2163.

With the use of a magnetometer the loss of the wire is measured at each frequency. The measurements are shown in Figure 3-6c in red where the offset of the line at the vertical axis corresponds to the frequency independent loss e.g. hysteresis loss and the inclination of the line represents the frequency dependent loss e.g. coupling and eddy current loss. The green and blue lines represent the theoretical calculated loss, considering hysteresis loss and coupling loss for two different values of j_c . The eddy-current loss is assumed to be negligible at this frequency ranges, which is strengthened by the founding of the previous validation. Since the literature reports different values of j_c for this particular wire, both theoretical results are shown in the plot.

Zhou et al. [40] derives the critical current from the magnetization loop which results in a value of $j_c = 2.1 \times 10^{10} A/m^2$ whereas Yang et al. [41] directly measured the critical current density at various field strength which resulted in a lower value of $j_c = 7 \times 10^9 A/m^2$.

At first glance the theoretical and experimental results have the same trend. The theory deviates from the measurements in with a range from -28% to +25%. Looking at the frequency dependent loss (inclination of the line) the theory and measurements are comparable however,

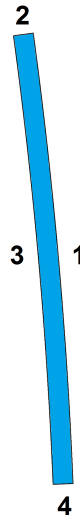


Figure 3-7 The four boundaries of the field windings at which the magnetic field distribution is copied from the 'field' model to the 'superconductor' model.

it is of no value to quantify the mismatch since the linearisation of the measurements is already a course fit.

In addition to the validation of the AC loss calculation, the comparison also gives good insight in the important parameters. The validation shows the critical current density j_c and the perpendicular matrix conductivity σ_{\perp} are of large influence on the accuracy of the calculations and therefore it is important to use reliable and accurate values for these parameters to get to a reasonable accurate result. Both parameters are difficult to measure and are depending on a lot of conditions. For instance, the perpendicular conductivity is influenced by the mechanical stress of the wire and the critical current density is depending on the temperature and magnetic field strength.

3-4 Numerical Methodology

Unfortunately the model that is used for the determination of the field distribution in the winding for the analytical calculations cannot directly be used for the numerical modeling of the AC loss. The problem is that the given boundary conditions, a uniform distribute current density, is conflicting with the current penetration boundary movement of the CSM model. The hysteresis loss, originates from the field penetration which is directly related tot the current penetration in the winding. The superconductor model has to be able to solve the current distribution so this uniform current distribution boundary condition cannot be applied. To work around this problem, first the magnetic field distribution in the machine is calculated using a uniformly distributed current density, after which the magnetic field at the borders of the field winding is copied to an other model, where the field winding is replaced by the superconductor model. Since the extracted magnetic field is enclosing the whole field winding, the induced current has to be equal to the applied current of the initial model.

The the magnetic field distribution, determined at the analytical calculations is extracted at the boundaries of a single field winding with Comsol with Matlab toopbox and the code

added in Appendix B. The boundaries are numbered and shown in Figure 3-7.

The magnetic field data can only be extracted in the Cartesian reference frame. However, the geometry of the winding is more convenient to describe in the cylindrical coordinate system since then there is only one variable needed for each boundary. Therefore the extracted xy-data is translated by multiplication with the rotation matrix to a cylindrical coordinate system, resulting in a radial and tangential field component. For the curved boundaries 1 and 3, only the tangential component of the field is of interest, and at the straight boundaries 2 and 4, only the radial component of the field is of interest. The code in Appendix B also includes a low pass filter which removes higher harmonics in the signal.

To get the total AC loss of the FEM calculations, the resistive heating is calculated in Comsol. This data is exported as a time signal after which the last period of the signal is averaged to get the AC loss for each field angle. It is important that the simulation is ran for the duration of the rotation of multiple pole-pairs since the initial magnetization of the winding increases the hysteresis loss drastically. Initial test-runs showed that after the rotation of about 3 pole pairs the AC loss is stabilized.

Results and Discussion

The structure of this chapter is following the steps of the methodology, where each result is accompanied with an explanatory and discussion section. First the calculation of the magnetic field distribution is treated. Second, the AC field due to time and space harmonics is shown followed by the result of the conversion in time and frequency domain. This AC field is translated to AC loss which leads to the final results of the analytical calculations. The AC loss components and the total AC loss with respect to field angle for both machine designs are shown at the end of this chapter, including the results of the numerical modeling.

4-1 Magnetic Field Distribution

The magnetic field distribution of both generator designs introduced in Figure 3-1 is calculated with Finite Element Method (FEM) software. This research made use of the rotating machinery toolbox developed by Comsol Multiphysics®. The result at a single time step and maximal torque is shown in Figure 4-1. The color scale represents the normalised magnetic flux density with a fixed range from -0.5T to 2T and the contour lines represent the magnetic vector potential in the direction of the normal vector of the cross section. The operation point of torque is realised by changing the angle between the rotor and armature magnetic field and is therefore referred to as the field angle. A field angle of 0° corresponds to 0Nm torque i.e. no load and a field angle of 90° corresponds to maximal torque.

A clear difference between the Non Magnetic Teeth (NMT) and Iron Teeth (IT) machine is visible in Figure 4-1. Apart from the different number of poles, also the iron teeth clearly concentrate the flux lines resulting in locally much higher flux density. The zoomed figures show a more detailed field distribution in the region of the field winding. The highest flux density is located at the edges of the field winding and the minimum value is in this particular case not located in the center of the winding due to field deformation caused by the 90° misalignment between rotor and armature field. The deformation of contour lines in the enlarged view of Figure 4-1c and 4-1d clearly illustrate interaction between rotor and armature, as if the armature field is pulling the rotor field forward.

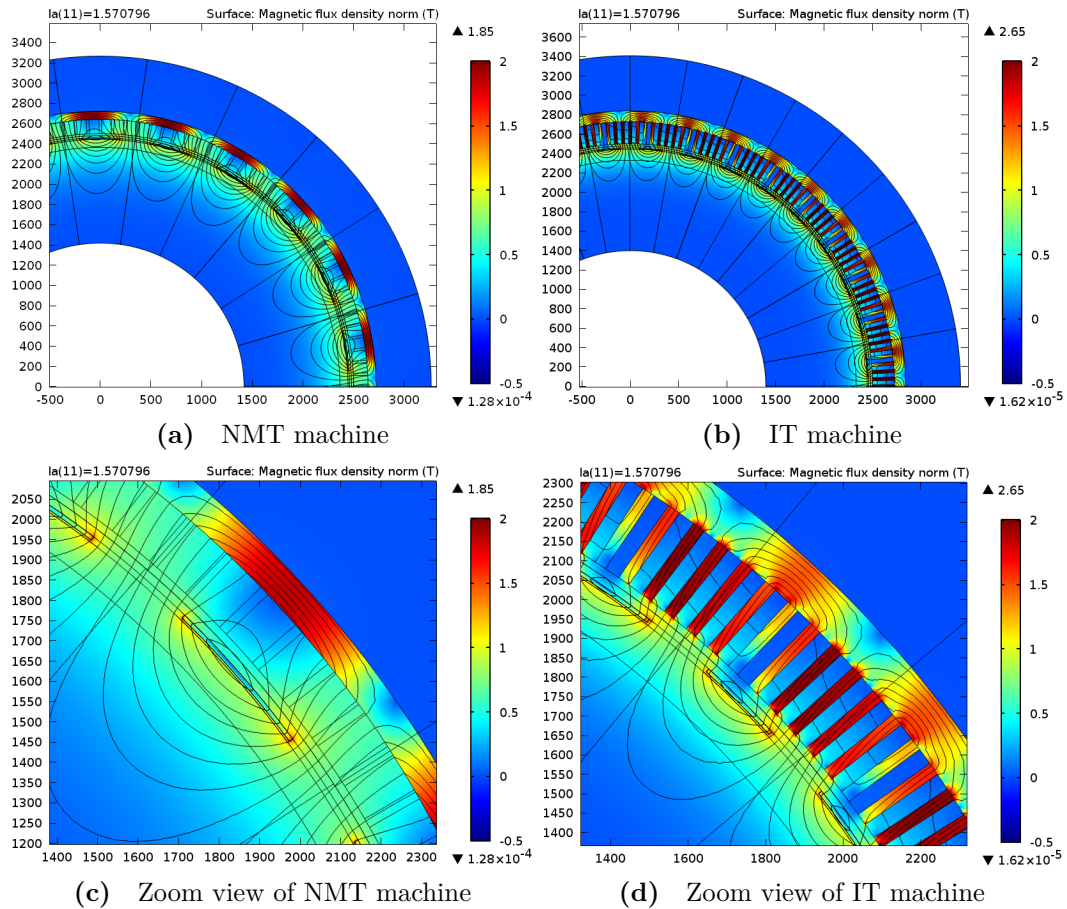


Figure 4-1 Surface plot of Magnetic flux density in the non-magnetic and iron teeth machine at maximal torque

Figure 4-2 shows the flux density distribution throughout the field winding in the reference frame of the rotor, where each group of lines is extracted at a different radius as is described in Section 3-2 and Figure 3-3. One group of lines consists of 200 lines, which is visualised by the zoom box, where every single line represents one time step. In total, one figure contains 2000 lines that describe the flux density distribution throughout the cross section of the field winding over the rotation of one pole in 200 time steps. The four plots show the result of the NMT and the IT machine in no-load and max-torque operation, although this research collected data from 11 load angles.

In no-load operation the magnetic flux distribution is symmetrical around the center of the field winding. Again, the plots at maximal torque show the field distribution is 'pulled' forward which is the result of the misalignment of the rotor and armature field. When looking at the difference between each time step it can be seen that for each plot the flux density has a large constant component (DC) and that the spread in time (AC) is much smaller at the NMT machine in comparison to the IT machine. The plots of Figure 4-2 are the first results that show the AC fields which the field winding is subjected to. The next section will zoom in on the AC signal by removing the DC component.

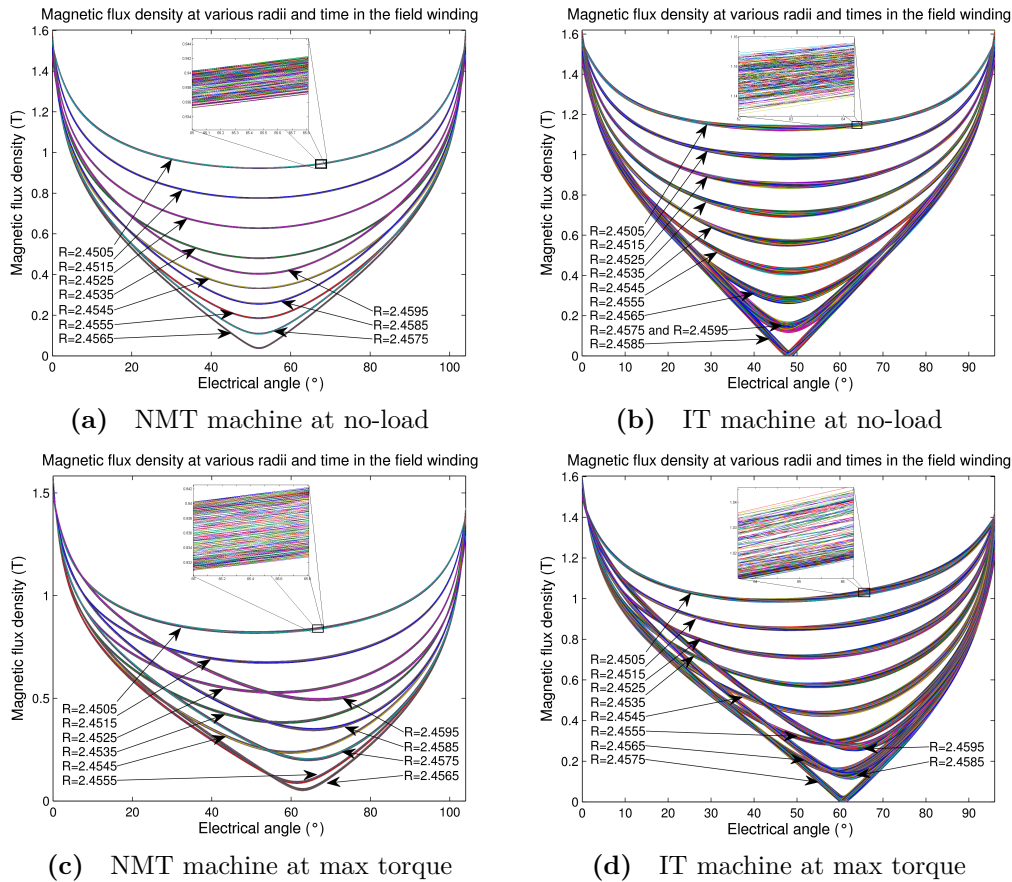


Figure 4-2 Magnetic flux density throughout the field winding. Each group of lines is taken at different radius in the field winding (Figure 3-3). The width of each group of lines represents the field change in time.

4-2 AC Field due to Space Harmonics

Figure 4-3a and 4-3b show the AC component of the magnetic flux density in time and Figure 4-3c and 4-3d show the same AC field in the frequency domain. All four plots are taken at the largest radius in the field winding and at maximal torque. Important to point out is that the AC field is seen from a reference frame of the field winding i.e. rotating with the same speed as the rotor.

Where the NMT machine shows a smooth waveform of small amplitude, the IT machine has a much larger amplitude and a clearly distorted wave form. The frequency spectrum of both machines shows the same. The NMT machine spectrum has a single peak at the 6th harmonic and a minor peak at the 12th harmonic. The IT machine on the other hand, shows much more harmonic content of which the 6th and the 12th harmonic frequencies are the largest.

Remarkable aspects of Figure 4-3 are that the amplitude of the AC field is not constant along the position in the winding. The 6th harmonic frequency is the first significant peak in the spectrum which can be explained by the design of the machine. Both machines are designed as a 3 phase machine meaning, the rotor will pass 6 armature windings over the rotation of one pole pair. The armatures are also designed with 2 slots per winding separated by a teeth

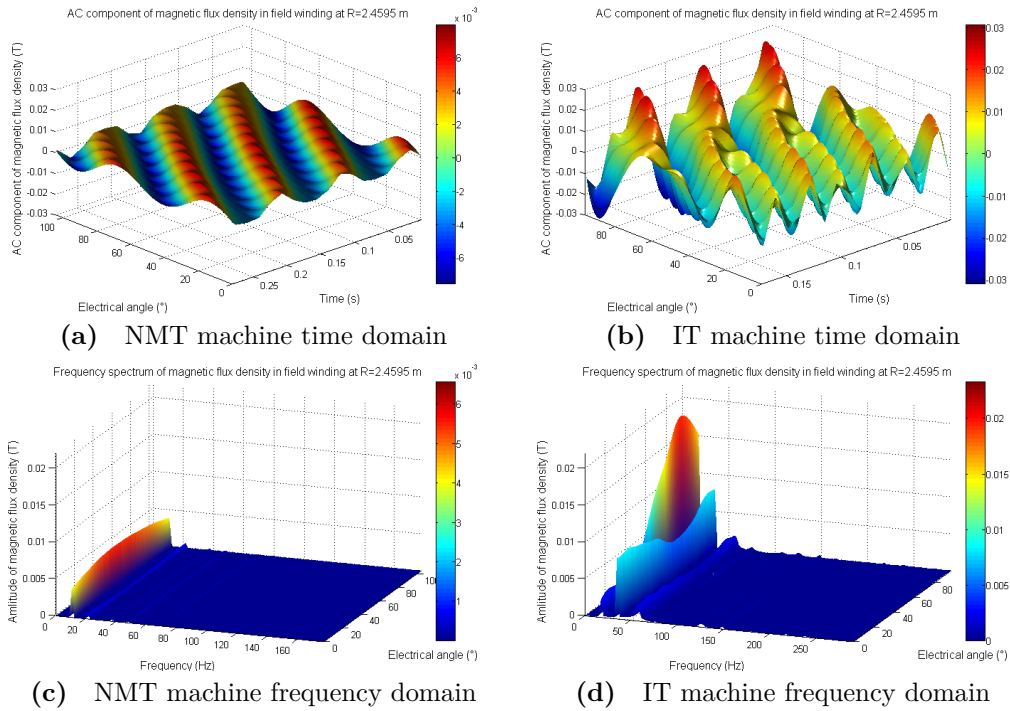


Figure 4-3 AC component of magnetic flux density in the field winding at the largest radius and maximal torque.

as can be seen in Figure 3-1. In the NMT machine this is not of large influence but in the IT machine, the effect of the armature slots is clearly shown by the amplitude of the 12th harmonic frequency.

From the AC field distribution, the peak-RMS value of the field and the relative penetration field β at each position in the winding is calculated. Figure 4-4 shows the value of β at maximal torque along the smallest radius in the field winding. The penetration field in the cylindrical and rectangular filament scenario is for all position angles larger than 1. In the NMT machine the scenario of merged filaments is continuous below 1. The scenario of merged filaments in the IT machine shows β is crossing unity (black line) which shows the importance of the decision point in the methodology. In other situation e.g. other torque and radii, the relative penetration of the cylindrical and rectangular filament scenarios also reaches below unity.

Section 3-2 described a method for calculating a frequency which represents the frequency of the largest AC loss contribution. Figure 4-5 shows the result of this method when applied on the data of Figure 4-3d. From the spectrum it can be clearly seen that at a position angle of 0° the 12th harmonic frequency is dominant and at about 70° the 6th harmonic frequency is dominant. The result of the frequency selection method is in agreement with these observations and shows a continuous smooth transition from one harmonic frequency to the other. At a position angle of 96° Figure 4-5 shows the 12th harmonic frequency is dominant again although the spectrum shows the amplitude of the 6th harmonic frequency is still larger. This demonstrates the method is calculating a frequency which represents the largest AC loss contribution and not the largest amplitude.

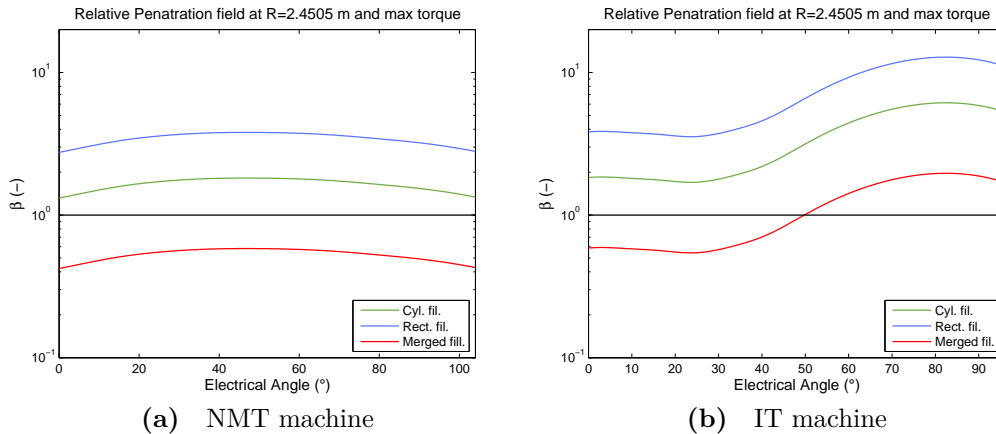


Figure 4-4 Relative penetration field β as function of the position angle in the field winding at the smallest radius in the field winding.

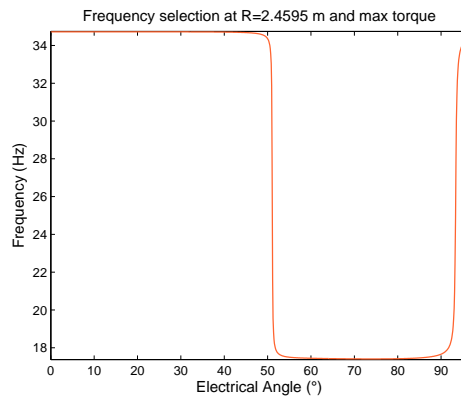


Figure 4-5 Result of frequency selection applied on IT machine at max torque, radius of R=2.4595m and $\beta > 1$.

4-3 AC Field due to Time Harmonics

A simulated waveform of the armature current is supplied by Dong Liu. Figure 4-6a and 4-6b shows the 3 phase armature current waveform and the distortion caused by the inverter in the time domain. The spectrum of the signal is shown in Figure 4-6c, 4-6d, 4-6e and 4-6f where the latter 3 plots are enlarged plots of the whole spectrum showing the fundamental frequency, harmonic content and inverter switching frequency.

The largest harmonic distortion is visible near a frequency of 1kHz which is therefore assumed to be the switching frequency of the inverter. The skin depth in copper at an operational temperature of 393K and 1kHz is 2.47mm. Since the thickness of the copper Electro Magnetic (EM) shield is larger than 4 times the skin depth it can be assumed the time harmonics are fully shielded and do not contribute to the AC loss in the field windings. This EM shield is only considered in the analysis of the time-harmonics and is not applied in the numerical model.

However, the spectrum of the armature current shows the amplitude of the harmonic content is only 0.5% of the fundamental frequency which could suggest the use of an EM shield might not be justified. In other words, is the AC loss contribution of the time harmonics

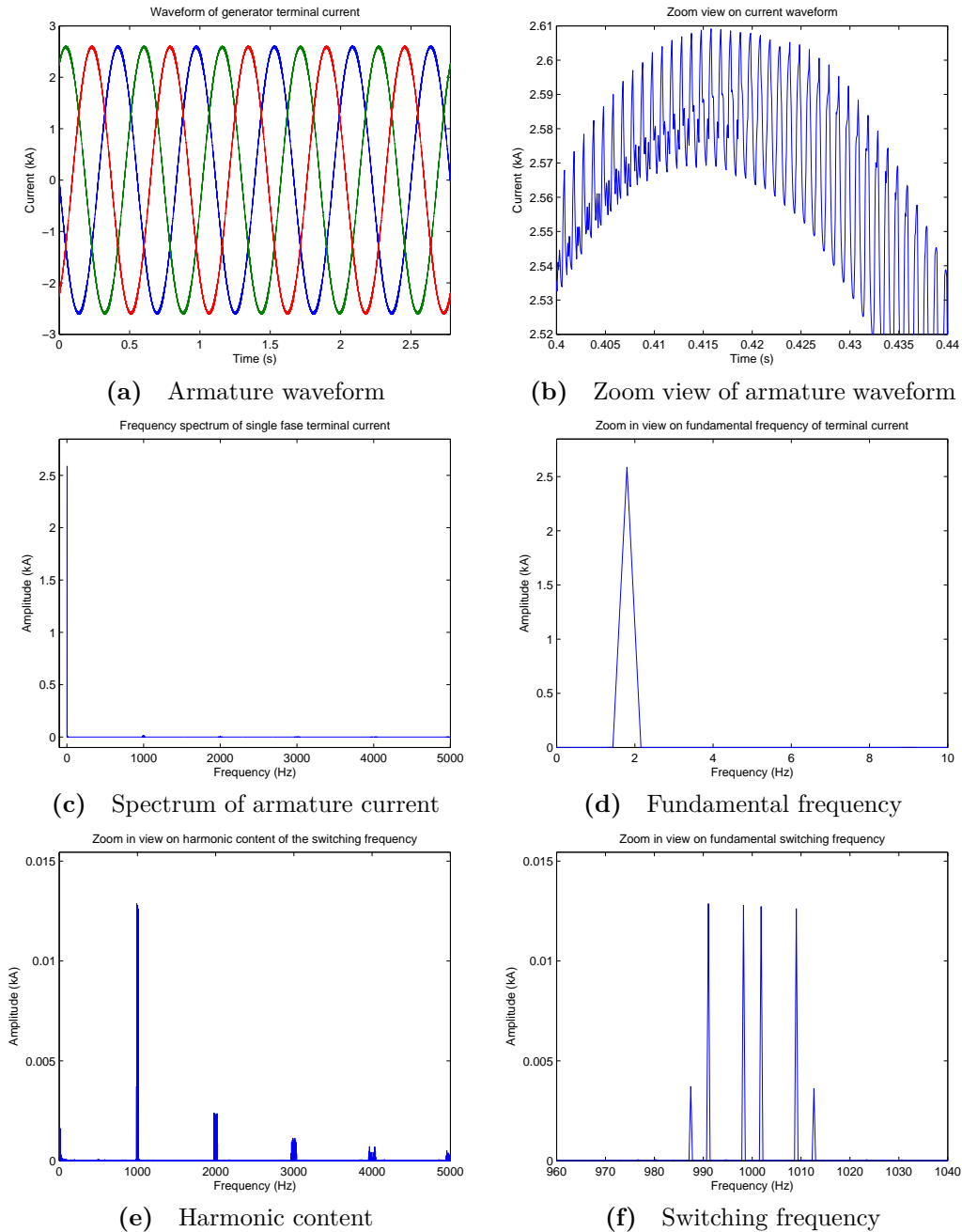


Figure 4-6 Armature current waveform and frequency spectrum at rated operation

significant compared to the AC loss caused by the space harmonics? To answer this question, the AC field caused by the time harmonics and experienced by the field windings needs to be determined. A calculation of the flux density distribution due to the fundamental frequency of the armature current is done and the peak value of the armature current produces an average flux density in the air gap of 0.15T in the NMT machine and 0.265T in the IT machine. Assuming the flux density scales linear with the current, the time harmonics then produce an AC field with an amplitude of 0.75mT in the NMT machine and 1.325mT in the IT machine. The average amplitude and frequency of the dominant space harmonic is 5mT at 10.6Hz in

the NMT machine and 19.1mT at 17.37Hz in the IT machine. When the superconductor is operating below penetration field this leads to an estimation of the time harmonics to be 30% of the space harmonic loss in the NMT machine and 1.9% of the AC loss in the IT machine. This already justifies the use of the EM shield. However, when the superconductor is operated above penetration field the time harmonic loss is 14 times the space harmonic loss in the NMT machine and 4 times the space harmonic loss in the IT machine. This estimation clearly shows the use of a 10mm copper EM shield is justified.

4-4 AC Loss in the Field Winding

In this section the hysteresis loss, eddy current loss and coupling loss, estimated in the analytical and numerical calculations, are discussed. Figure 4-7 shows the analytical hysteresis loss throughout the field winding at no load and max torque operation for both machine designs and for the scenario of cylindrical filaments. These plots show the hysteresis loss is varying along the cross section of the field winding. The scale of the z-axis is important to notice since the hysteresis loss in the NMT machine is in the order of 10 times smaller than the loss in the IT machine. The loss distribution throughout the windings cross section is strongly dependent on the operational point.

The shape of the hysteresis loss in the NMT machine at maximal torque (Figure 4-7c) is the same as the shape of the largest amplitude in the spectrum shown in Figure 4-3c. This can be explained by the spectrum in combination with a relative penetration field which is constantly above 1. Throughout the winding's cross section the dominant frequency is the 6th harmonic and $\beta > 1$ resulting in a loss that is linear with the amplitude of the AC field.

The analytical hysteresis loss distribution in the IT machine shows a different shape when compared to the spectrum of Figure 4-3d because in this machine the dominant frequency is changing throughout the windings cross section. The surface plot of Figure 4-7d shows the dominant frequency switches at the point where the hysteresis loss in both frequencies is equal as can be seen by the discontinuity at the center of the plot. This line is located at a position angle just above 50° which also can be seen in Figure 4-5.

The total hysteresis loss in the superconducting winding of the generator is obtained by integrating the hysteresis loss over the winding's cross section and multiplying with the total superconductor volume in the machine. This is done for each generator design, each field angle, each type of loss and for three different relative penetration fields: $\beta < 1$, $\beta > 1$ and combined β . The combined β is the result of the described methodology which evaluates β for each position in the field winding. The results of only using the equations for $\beta < 1$ and $\beta > 1$ are added to show the effect of selecting the correct conditions. The numerical calculations do not consider the relative penetration field explicitly thus a single line of the FEM result is shown.

Each AC loss component in the NMT machine is plotted in Figure 4-8a, 4-8c and 4-8e as function of the field angle. The hysteresis loss in the NMT machine, is increasing with the field angle and ranging from 13.7W up to 266W. The difference between each scenario is caused by the different perpendicular thickness of the filaments i.e. the difference in penetration field. The cylindrical filament scenario is operated slightly above penetration field with β ranging from 1.3 to 2.3 where the hysteresis loss is close to the maximum loss (Figure 2-8). The

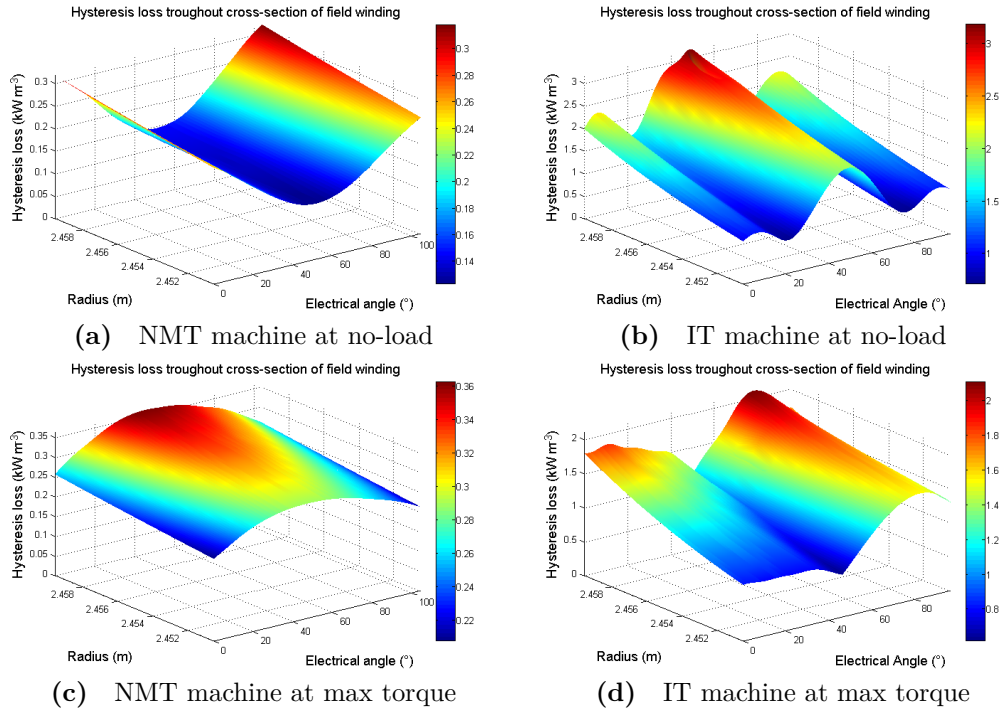
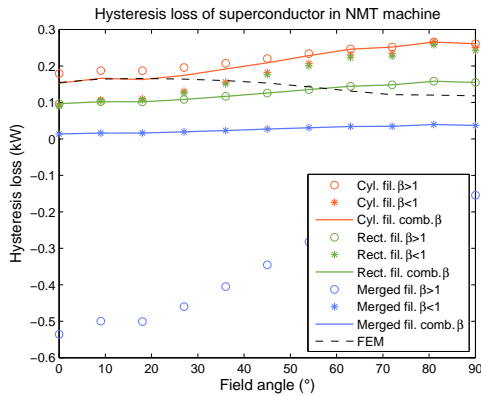


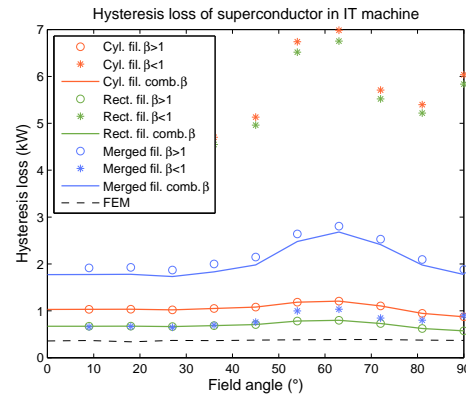
Figure 4-7 Analytically calculated hysteresis loss per unit volume of the cylindrical filament scenario throughout the field winding cross-section

rectangular filament geometry is operated at a larger β ranging from 2.7 to 4.8 where the hysteresis loss is lower. The merged filament geometry on the other hand is operated below penetration field with β values from 0.42 to 0.73 where the hysteresis loss is at its maximum according to Figure 2-8. However, the large thickness of the merged filament scenario causes the total loss to be lower than the other scenarios. A remarkable result of Figure 4-8a is the theoretical result of the merged filaments below penetration field (blue circles) which are negative. A negative loss is obviously not possible. This result is negative because the used equations are only valid for $\beta > 1$ which is not the case at these field strengths and scenario.

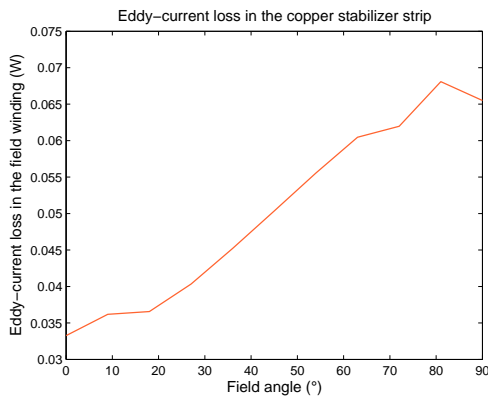
The numerical calculations only show results of the hysteresis loss since the model only contains the superconductor material. The eddy-current loss and coupling loss are generated in the normal metal regions of the wire and hence are not include. The numerical calculated hysteresis loss of the NMT machine shown in Figure 4-8a together with the analytical results for comparison. The results show a slight decreasing trend with respect to an increasing field angle. The absolute value of the loss is ranging from 118W to 166W which is in the same range as the analytical results. A point of discussion is the modeled geometry since the superconductor model consists of a single merged block of superconductor, while the analytical calculations assumed individual wires which allows for field penetration in the winding due to the normal metal regions. The difference is the numerical model attempts to shield the magnetic field around the whole winding, although in reality the flux lines will also pass through the winding reducing the total magnetization. How much the hysteresis loss due to the space harmonics is influenced by this assumption is difficult to say. Certainly the numerical hysteresis loss will not increase when the wires in the winding are modeled individually. Therefore, this numerical result can be regarded as the upper boundary of the hysteresis loss.



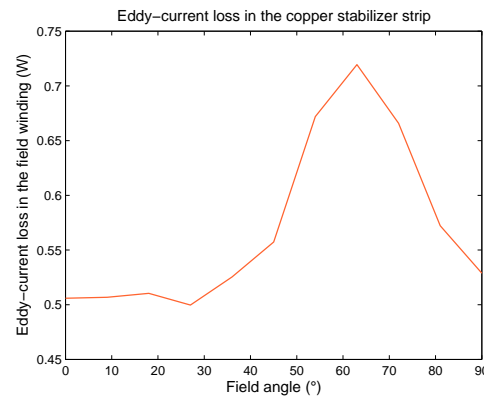
(a) Hysteresis loss, NMT machine



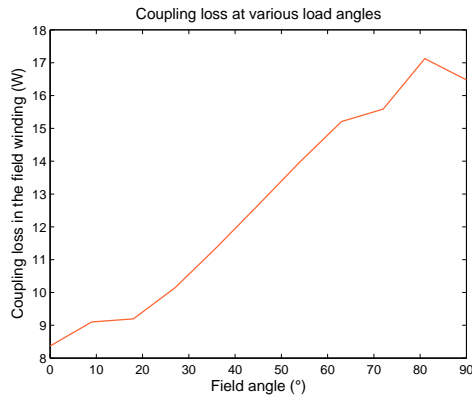
(b) Hysteresis loss, IT machine



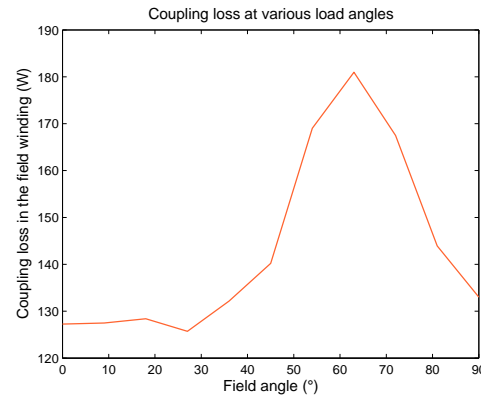
(c) Eddy current loss, NMT machine



(d) Eddy current loss, IT machine



(e) Coupling loss, NMT machine



(f) Coupling loss, IT machine

Figure 4-8 AC loss components in the full machine as function of the torque. Hysteresis loss is displayed per scenario. Eddy current loss and coupling loss are not influenced by the various scenarios or relative penetration field.

The eddy current loss and coupling loss in the NMT machine have the same trend as the hysteresis loss which is an increasing loss with the field angle. The eddy current loss can be neglected since it is less than 0.2% of the total AC loss. The coupling loss is responsible for about 5% of the total loss in the cylindrical filament scenario and up to 36% of the total loss in merged filament scenario.

The Figures 4-8b, 4-8d and 4-8f show each AC loss component in the IT machine. Due to larger

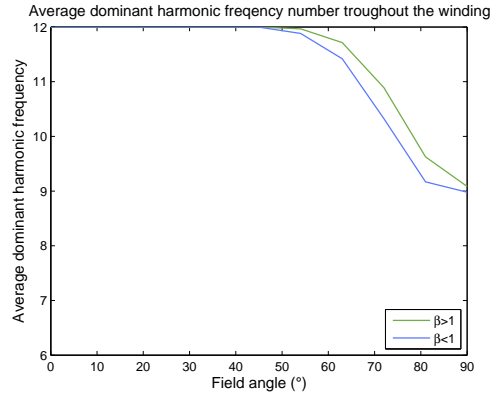


Figure 4-9 The average dominant harmonic frequency over the field winding in the IT machine.

space harmonics at higher frequencies (Figure 4-3), each loss component in the IT machine is larger compared to the NMT machine. The hysteresis loss for the various scenarios is ranging from 570W to 2.68kW. The cylindrical and rectangular filament geometries are continuously operated above penetration and the merged filament geometry is in some regions operated above penetration and others below penetration as can be seen from the blue line, positioned slightly below the blue circles.

The numerical hysteresis loss in the IT machine does not show a clear trend with respect to the field angle. The numerical hysteresis loss is smaller than all analytical results and ranging from 341W to 387W. Compared to the numerical hysteresis loss of the NMT machine this is on average 2.5 times larger. The numerical hysteresis loss differs from the analytical initially because the assumptions are different and secondly because current density distribution is different in the superconductor.

In contrast with the trend seen in the NMT machine, the trend of the AC loss in the IT machine is not increasing with the field angle. For field angles from 0° up to around 50° the loss is increasing with the field angle but at higher field angles the loss is decreasing again. This is probably caused by the change of average dominant frequency as the field angle increases. Figure 4-9 shows the average dominant harmonic frequency as function of the field angle in the IT machine and this supports the explanation. At low field angles, clearly the 12th harmonic frequency is dominant throughout the whole cross section of the winding. However, as the field angle increases, the 6th harmonic frequency comes up as the dominant frequency in some regions of the field winding, shifting the average dominant frequency down. This process begins at a field angle of around 50° and at maximal torque both frequencies are equally dominant shifting the average dominant frequency to the center between the 12th and the 6th harmonic frequency.

Again, the eddy current loss in the IT machine is negligible since it contributes less than 0.1% to the total loss in the machine. The coupling loss in the IT machine is responsible for around 5% up to 14% of the total AC loss.

Conclusions and Recommendations

5-1 Conclusions

An overview of the basics of superconductivity with a focus on AC loss is given in Chapter 2. Remarkable is the Meissner effect where shielding currents divert the magnetic flux lines out of the superconductor. Above a certain field strength the magnetic flux lines start to penetrate the superconductor. Bean's critical state model describes the behaviour of superconductors on a macroscopic scale, which makes it useful for describing the magnetic field penetration in boundary motion and overall loss calculations. The magnetic field strength at which the penetration boundary reaches to the center of the superconductor is referred to as the penetration field. When a transport current is present the effective penetration field is lowered which could have a positive or negative effect on the AC loss depending on the amplitude of the magnetic field. All loss equations are separated into two domains of magnetic field: 1) field is smaller than the penetration field and 2) field is equal or larger than the penetration field.

AC loss in a superconducting wire can be categorised into four loss mechanisms.

1. Hysteresis loss
2. Eddy current loss
3. Coupling loss
4. Ferromagnetic loss

The hysteresis loss occurs in the actual superconductor material when penetrated magnetic flux lines move through the material. Each quantised unit of flux is surrounded by a current vortex, pinning it in place. At the center of each vortex lays a non-superconducting core. As the flux lines move through the superconductor, the pinning force is overcome, hence work

is done. Additionally, the current surrounding the flux lines moves partly through the non-superconducting core resulting in resistive loss. The magnetization of superconductors is an hysteric effect due to these flux motions and is therefore referred to as hysteresis loss.

For strength and stability a multifilament superconducting wire also contains normal metal materials. Eddy current loss occurs in the normal metals of a wire and originates from the resistive loss of the induced currents. In the filamentary region also eddy current like loss is generated inside the alloy matrix surrounding the filaments. However, these currents are referred to as coupling currents since the presence of the superconducting filaments influence their path. Coupling currents run transverse to the filament length and could cross through a filament or travel around the filaments depending on the inter filament conductivity. Ferromagnetic loss is referring to the hysteresis loss in the ferromagnetic materials of the wire, with exception of the superconductor material. Ferromagnetic loss is caused by the hysteric magnetization of the ferromagnetic materials. All four loss mechanisms are relevant in this project, however, at low frequencies, the eddy current loss is much smaller than the hysteresis loss.

The use of a copper Electro Magnetic (EM) shield is justified and reduces the AC loss in the field windings significantly. A rough estimation shows that without EM shielding, the AC loss in the field windings is up to 14 times larger under certain conditions due to the time harmonics. A thickness of 10mm is sufficient to attenuate the time harmonics with more than 98%.

The numerically calculated hysteresis loss in the NMT machine is ranging from 118W to 166W where the trend shows a decreasing loss with respect to an increasing torque. The numerical results of the IT machine show a hysteresis loss which is on average 2.5 time larger, ranging from 341W to 387W.

To analyse the hysteresis loss of a multi-frequency field, a method is derived which determines a surrogate frequency and amplitude that represents the biggest AC loss contribution in that field. A validation of the analytical equations is done by comparing experimental results with calculated results of the same set up. The experiment is done on a sample of multifilament Magnesium diboride (MgB_2) wire in a transverse magnetic field, oscillating between 1T and 3T at a frequency range from 0Hz to 20mHz. The theoretical and experimental results show the same trend and the error between the theory and the measurements ranges from -28% to +25%.

The amplitude of the space harmonics in an Iron Teeth (IT) machine are larger than the space harmonics in a Non Magnetic Teeth (NMT) machine. Also the frequency spectrum of the space harmonics in the IT machine contains more energy in the higher harmonic frequencies compared to the NMT machine. A remarkable result is that the dominant frequency in the IT machine changes throughout the field winding. At a large radius, close to the armature and iron teeth, the 12th harmonic frequency is dominant while at further distances from the armature the 6th harmonic frequency is dominant.

Throughout the cross section of the field winding the AC loss is varying. The location of the largest AC loss contribution is depending on the torque, teeth material and superconductor filament shape. In the NMT machine the total AC loss at no load operation is on average 50% of the AC loss at maximal torque and is ranging from 22.2W to 283W depending on the filament geometry and torque. The total AC loss in the IT machine shows a different trend

with increasing torque due to a change in dominant frequency as the torque becomes larger. The AC loss in the IT machine is on average 10.6 times larger than the AC loss in the NMT machine and ranges from 0.7kW to 2.9kW. When comparing the costs of active material with the loss of both designs the conclusion is that the machine with the lowest material costs, the IT machine is requires a much larger and therefore more expensive cooling.

Since the eddy current loss in both machines is less than 0.2% of the total AC loss, this loss is negligible in these machines. The coupling loss is responsible for 5% up to 36% of the total AC loss and therefore cannot be neglected.

5-2 Recommendations

Each analytical calculation of the AC loss in a superconducting machine requires assumptions. The AC loss is strongly depending on the critical current density of the used wire and the inter filament conductivity or perpendicular conductivity of the filamentary region. Therefore to have a accurate AC loss calculation, these parameters need to be available with high accuracy. Therefore it is recommended to measure the inter filament conductivity and critical current density on a sample wire in wound conditions once available.

This thesis partly validates the used equations or methodology. However, the multi-frequency AC loss calculation is not validated because there was no experimental data available using multiple frequencies. In order to validate the complete methodology it is recommended to do an extensive validation covering a frequency range from the fundamental till the 12th harmonic and multiple amplitudes needs to be done to determine the performance of the multi-frequency method. This could be done in an experiment where a section of superconducting wire is simultaneously exposed to two external fields with different frequency.

In determining the space harmonics, the EM shield is neglected since it is primarily designed to reduce the high frequency time harmonics. However, the copper shield will also attenuate the low frequency space harmonics and therefore reduce the overall AC loss in the field winding. A short calculation shows at an frequency of 10.6Hz the amplitude of the space harmonics will reduce with 40%. However, what the effect will be on the total AC loss in the field windings is more difficult to judge and therefore needs more research, taking into account the position of the shielding, operational temperature and reluctance of the copper.

Current analytical results are obtained with assuming a uniform current distribution in the winding. In reality the current distribution is probably not uniform due to shielding effect. The current superconductor model can be extended by modeling the individual wires of a winding. Although this requires much more computational force, the result will give insight to the current distribution in the wire. Additionally, to improve the superconductor model and locate the important variables, a parameter sensitivity analysis should be done.

Bibliography

- [1] Columbus Superconductors, “MgB2 Sandwich Wire Properties,” 2013.
- [2] P. Langevin, *La théorie du rayonnement et les "quanta" : rapports et discussions de la réunion tenue à Bruxelles, du 30 octobre au 3 novembre 1911*. Paris: Gauthier-Villars, 1912.
- [3] K. H. Bennemann and J. B. Ketterson, *Superconductivity: Conventional and Unconventional Superconductors*. Berlin, Heidelberg: Springer Berlin Heidelberg, 2008.
- [4] M. Garber, M. Suenaga, W. B. Sampson, and R. L. Sabatini, “Critical Current Studies on Fine Filamentary NbTi Accelerator Wires,” in *Advances in Cryogenic Engineering Materials SE - 84* (R. P. Reed and A. F. Clark, eds.), vol. 32 of *Advances in Cryogenic Engineering Materials*, pp. 707–714, Springer US, 1986.
- [5] W. J. J. Carr, *AC loss and macroscopic theory of superconductors*. London [etc.]: London etc. : Taylor & amp, 2001.
- [6] M. N. Wilson, *Superconducting magnets*. Oxford : New York [etc.]: Oxford : Clarendon Press, 1983.
- [7] T. Ogasawara, Y. Takahashi, K. Kanbara, Y. Kubota, K. Yasohama, and K. Yasukochi, “Transient field losses in multifilamentary composite conductors carrying dc transport currents,” *Cryogenics*, vol. 20, pp. 216–222, Apr. 1980.
- [8] C. Y. Ho, M. W. Ackerman, K. Y. Wu, T. N. Havill, R. H. Bogaard, R. A. Matula, S. G. Oh, and H. M. James, “Electrical Resistivity of Ten Selected Binary Alloy Systems,” *Journal of Physical and Chemical Reference Data*, vol. 12, p. 183, Apr. 1983.
- [9] R. Edwards, “The Magnetic Properties of Evaporated Nickel and Iron Films,” *Physical Review*, vol. 29, pp. 321–331, Feb. 1927.
- [10] P. C. Sen, *Principles of electric machines and power electronics*. New York [etc.]: New York etc. : Wiley, 1997.

- [11] M. Majoros, M. Bhatia, M. D. Sumption, S. Kawabata, M. Tomsic, M. Rindfleisch, E. W. Collings, U. B. Balachandran, K. Amm, D. Evans, E. Gregory, P. Lee, M. Os-
ofsky, S. Pamidi, C. Park, J. Wu, and M. Sumption, “AC TRANSPORT CURRENT
AND APPLIED MAGNETIC FIELD LOSSES IN MgB₂ MULTIFILAMENTARY
STRANDS WITH NON-MAGNETIC SHEATH MATERIALS,” *AIP Conference Pro-
ceedings*, vol. 986, pp. 388–395, 2008.
- [12] Vestas Wind Systems A/S, “Vestas OFFSHORE brochure,” (Aarhus), p. 16, Vestas,
2013.
- [13] D. W. Hazelton, V. Selvamanickam, J. M. Duval, D. C. Larbalestier, W. D. Markiewicz,
H. W. Weijers, and R. L. Holtz, “Recent Developments in 2G HTS Coil Technology,”
IEEE Transactions on Applied Superconductivity, vol. 19, pp. 2218–2222, June 2009.
- [14] Innwind.eu, “T 3.1 - Superconducting direct drive generators -,” 2014.
- [15] C. Buzea and T. Yamashita, “Review of the superconducting properties of MgB₂,”
Superconductor Science and Technology, vol. 14, pp. R115–R146, Nov. 2001.
- [16] Elsevier B.V., “Scopus - Document search,” 2014.
- [17] G. Rubinacci, F. Villone, and W. Zamboni, “Validation of a 3D macroscopic model for
superconductors,” *COMPEL: The International Journal for Computation and Mathe-
matics in Electrical and Electronic Engineering*, vol. 24, no. 2, pp. 546–557, 2005.
- [18] B. Turck and L. Zani, “A macroscopic model for coupling current losses in cables made
of multistages of superconducting strands and its experimental validation,” *Cryogenics*,
vol. 50, pp. 443–449, Aug. 2010.
- [19] J. Kötzler, G. Nakielski, M. Baumann, R. Behr, F. Goerke, and E. Brandt, “Universality
of frequency and field scaling of the conductivity measured by ac susceptibility of a
YBa₂Cu₃O₇ film,” *Physical Review B*, vol. 50, pp. 3384–3391, Aug. 1994.
- [20] S. Blundell, *Superconductivity, A very Short Introduction*. Oxford: Oxford University
Press, 2009.
- [21] D. Goodstein and J. Goodstein, “Richard Feynman and the History of Superconductiv-
ity,” *Physics in Perspective*, vol. 2, pp. 30–47, 2000.
- [22] H. Kamerlingh Onnes, “Sur les résistances électriques,” *Communications from the Phys-
ical Laboratory of the University of Leiden*, vol. 29, pp. 1–11, 1911.
- [23] H. B. G. Casimir and H. B. G. Casimir, *Haphazard Reality: Half a Century of Science*.
2010.
- [24] J. W. Rohlf and P. J. Collings, “Modern Physics from α to Z[^{sup} \hat{A}],” *Physics Today*,
vol. 47, p. 62, Jan. 1994.
- [25] S. Sarangi, S. P. Chockalingam, R. G. Mavinkurve, and S. V. Bhat, “Experimental
Evidence for Zero DC Resistance of Superconductors,” p. 7, June 2005.
- [26] K.-H. Müller, “AC power losses in flexible thick-film superconducting tapes,” *Physica C:
Superconductivity*, vol. 281, pp. 1–10, July 1997.

- [27] D.-X. Chen and R. B. Goldfarb, “Kim model for magnetization of type-II superconductors,” *Journal of Applied Physics*, vol. 66, p. 2489, Sept. 1989.
- [28] E. M. Gyorgy, R. B. van Dover, K. A. Jackson, L. F. Schneemeyer, and J. V. Waszczak, “Anisotropic critical currents in Ba₂YCu₃O₇ analyzed using an extended Bean model,” *Applied Physics Letters*, vol. 55, p. 283, July 1989.
- [29] F. Grilli, E. Pardo, A. Stenvall, D. N. Nguyen, and F. Gomory, “Computation of Losses in HTS Under the Action of Varying Magnetic Fields and Currents,” *IEEE Transactions on Applied Superconductivity*, vol. 24, pp. 78–110, Feb. 2014.
- [30] J. Bardeen and M. J. Stephen, “Theory of the Motion of Vortices in Superconductors,” *Physical Review*, vol. 140, pp. A1197–A1207, Nov. 1965.
- [31] N. Amemiya, F. Kimura, and T. Ito, “Total AC Loss in Twisted Multifilamentary Coated Conductors Carrying AC Transport Current in AC Transverse Magnetic Field,” *IEEE Transactions on Applied Superconductivity*, vol. 17, pp. 3183–3186, June 2007.
- [32] F. Fiorillo, *Characterization and Measurement of Magnetic Materials*. Amsterdam: Elsevier B.V., first ed., 2004.
- [33] W. Carr, “Electromagnetic theory for filamentary superconductors,” *Physical Review B*, vol. 11, pp. 1547–1554, Feb. 1975.
- [34] Massachusetts Institute of Technology. Cryogenic Engineering Laboratory.; Massachusetts Institute of Technology. Electric Power Systems Engineering Laboratory., *Demonstration of an advanced superconducting generator : interim report for the period August 15, 1977-December 15, 1978*. Cambridge: Massachusetts Institute of Technology Industrial Liaison Program, 1978.
- [35] A. Campbell, “A general treatment of losses in multifilamentary superconductors,” *Cryogenics*, vol. 22, pp. 3–16, Jan. 1982.
- [36] M. P. Oomen, J. Rieger, M. Leghissa, and H. H. J. ten Kate, “Field-angle dependence of alternating current loss in multifilamentary high-T_c superconducting tapes,” *Applied Physics Letters*, vol. 70, p. 3038, June 1997.
- [37] Comsol Multiphysics, “Superconducting Wire - COMSOL,” 2014.
- [38] D. Liu, “Comparison of 10MW Superconducting Generator Topologies for Wind Turbines,” tech. rep., Delft University of Technology, Delft, 2014.
- [39] M. Dhallé, “201100214 Applications of Superconductivity Problem session 3,” 2011.
- [40] C. Zhou, W. Offringa, A. Bergen, W. A. J. Wessel, H. J. G. Krooshoop, M. Dhallé, M. D. Sumption, E. W. Collings, M. Rindfleisch, M. Tomsic, H. H. J. ten Kate, and A. Nijhuis, “Intra-wire resistance and AC loss in multi-filamentary MgB₂ wires,” *Superconductor Science and Technology*, vol. 26, p. 025002, Feb. 2013.
- [41] Y. Yang, M. Susner, M. D. Sumption, M. Rindfleisch, M. Tomsic, and E. W. Collings, “Influence of Strand Design, Boron Type, and Carbon Doping Method on the Transport Properties of Powder-in-Tube MgB₂-XCX Strands,” p. 35, Sept. 2011.

Appendix A

Assignment with Experimental Data

Problem 1: Magnetization / AC losses in strands

In collaboration with a wire producer, EMS studies various properties of state-of-the-art MgB_2 conductors. One of these properties is AC loss. To measure the loss we use a magnetometer in which 1.8m-long wire samples are cooled to 4.2K and submitted to time-varying perpendicular magnetic fields. With a compensated sensing coil-set and a superconducting integrator the magnetic moment m of the sample is registered as a function of externally applied magnetic induction B (figure 1).

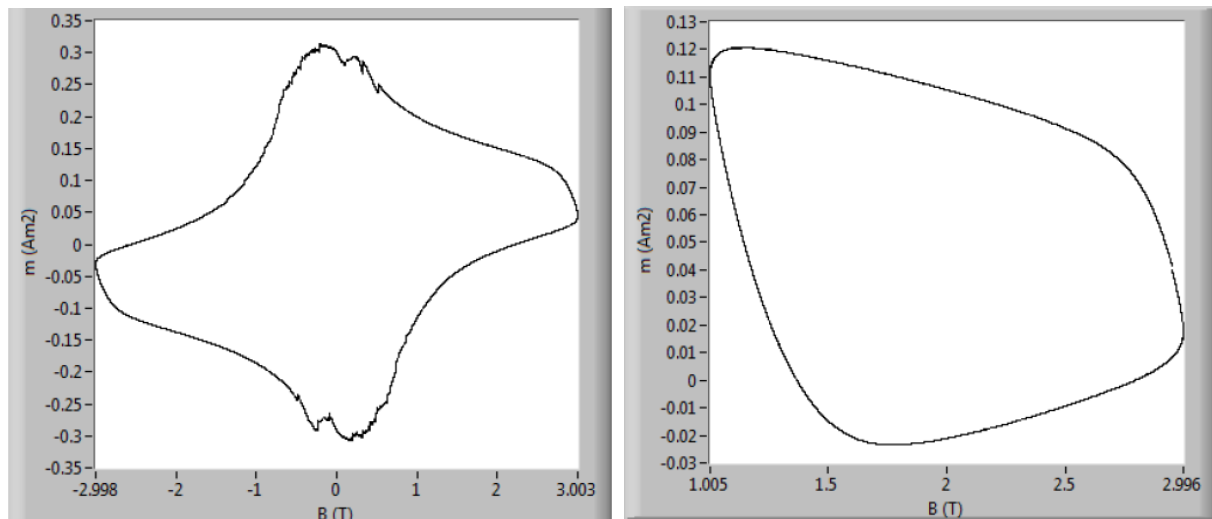


Figure 1: (left) Magnetization loop of MgB_2 prototype wire #2163 measured between ± 3 T at $T = 4.2\text{K}$ with a frequency of $f = 2$ mHz. **(right)** Minor loop of the same sample measured under the same conditions but this time between 1 and 3T.

Already early on in this project, it became clear that – compared to Nb_3Sn or NbTi – these wires are prone to flux jumps, especially at low applied magnetic field (figure 1, left; *N.B. why are these wires less stable (see also figure 3 and table 1)?; why only at low field?*).

Thermal stability is determined by filament size, critical current density and the possibility of heat transfer to the environment (cooling). Compared to LTS, in these wires the filaments are relatively large and sheathed with a Nb layer which conducts heat relatively poorly. This becomes an issue especially at low magnetic field because the critical current density is higher there.

Since we're mostly interested in a systematic comparison between the different wires within this experimental series, we decided to collect the necessary data from minor loops between $B = 1$ and 3T, thus avoiding the unstable low-field regime (figure 1, right).

Question 1a)

- From figure 1 right, work out the irreversible magnetization ΔM of wire sample #2163 at $T = 4.2\text{K}$; $B = 2\text{T}$; and ramp rate 8mT/s . Sample details can be found in table 1 below.

A quick check shows that the figure on the right indeed corresponds to a ramp-rate of 8mT/s : the total field 'trajectory' in a $1\text{T} > 3\text{T} > 1\text{T}$ cycle is $2 \times 2\text{T} = 4\text{T}$. The period of such a cycle is $1/f = 1/(2 \cdot 10^{-3}\text{Hz}) = 500\text{s}$ (see figure caption), so that the ramp rate is $4\text{T}/500\text{s} = 8\text{mT/s}$.

The y-axis of the figure gives the magnetic moment m [Am^2] instead of the magnetization M [Am^{-1}] (the magnetometer doesn't 'know' the size of the sample and gives the magnetic dipole moment it 'sees', just like a multimeter measures the resistance R of a given sample and not the resistivity ρ).

To convert one into the other, we need to use the relation $M = \frac{m}{V}$, with V the sample volume: the magnetization can be seen as a 'dipole moment density', see e.g. Griffiths §6.1.4.

The sample volume $V = \ell \pi \left(\frac{d_w}{2} \right)^2$ with ℓ the sample length (1.8m, see higher) and d_w the wire diameter (0.83mm, see table 1). Filling in the numbers gives $V = 9.7 \cdot 10^{-7} \text{ m}^3$.

The hysteretic magnetization loop has two branches, one for increasing field ($\dot{H} > 0$) and one for decreasing field ($\dot{H} < 0$). For $\dot{H} > 0$, we find at $\mu_0 H = 2\text{T}$ a moment $m_+ \approx -0.02 \text{ Am}^2$ and therefore a magnetization $M_+ \approx -2.1 \cdot 10^4 \text{ Am}^{-1}$. For decreasing field $\dot{H} < 0$, we have at 2T $m_- \approx +0.11 \text{ Am}^2$ and $M_- \approx 1.1 \cdot 10^5 \text{ Am}^{-1}$. The irreversible magnetization ΔM is defined as the difference between these two branches $\Delta M = M_- - M_+ \approx 1.3 \cdot 10^5 \text{ Am}^{-1}$.

- Still based on figure 1, estimate the volumetric loss density (in J/m^3) that is generated in this wire when it runs through a cycle $1 \rightarrow 3 \rightarrow 1\text{T}$. Compare your estimate with figure 2 below.

The loss generated during such a closed cycle is $E = \oint M dB$ (slide 14, lecture 5) which, after proper normalization of the y-axis to go from moment m to magnetization M (see above), the surface area enclosed by the loop in figure 1, right. A rough estimate of this surface area is given by $E \approx \Delta M \Delta B = 1.310^5 \text{ Am}^{-1} \times 2\text{T} = 2.6 \cdot 10^5 \text{ Jm}^{-3} = 260 \text{ kJm}^{-3}$. Compared with the relevant data point in figure 2 ($E = 230 \text{ kJm}^{-3}$, obtained by numerical integration of figure 1), our rough estimate is reasonably close.

Question 1b)

- Work out the critical current density J of the wire at 4.2K; 2T.
- Compared to typical values for the (transport) critical current density of technical superconductors, presented in earlier lectures, is this a reasonable number?
- Did you obtain J_e or J_c ?
- The hysteresis in the magnetization is caused by flux pinning in the superconducting filaments. The Bean critical state description (slides 3-5, lecture 5) shows that the magnetization at full flux penetration of cylindrical filaments in a perpendicular field is $M = \pm \frac{2}{3\pi} J_c d_f$ (slide 6, lecture 5), with d_f the filament diameter and the sign on the right of the equation depending on the direction of

the external field ramp (“-” for $\dot{H} > 0$ and “+” for $\dot{H} < 0$)¹. The irreversible magnetization ΔM calculated in problem 1a therefore corresponds to twice this value: $\Delta M = \frac{4}{3\pi} J_c d_f$. Rearranging this relation gives $J_c = \frac{3\pi \Delta M}{4 d_f}$, which allows to calculate J_c from the measured ΔM provided that we know the filament diameter.

Geometrical considerations show that $A_f = \pi \left(\frac{d_f}{2} \right)^2 = \frac{A_{sc}}{N} = \frac{\lambda A_w}{N} = \frac{\lambda}{N} \pi \left(\frac{d_w}{2} \right)^2$; with A_f , A_{sc} and A_w the cross-sectional areas of filament, superconducting material and wire; λ the filamentary fill-factor and N the number of filaments. This equation can be simplified to $d_f = \sqrt{\frac{\lambda}{N}} d_w$. Filling in the numbers such from table 1 gives for wire #2163 $d_f \approx 100 \mu\text{m}$, in good agreement with the micrograph shown in figure 3.

Combining $\Delta M \approx 1.3 \cdot 10^5 \text{ Am}^{-1}$ from problem 1a with the $d_f \approx 10^{-4} \text{ m}$ just found yields with the aid of the critical state formula discussed above $J_c \approx 3.1 \cdot 10^9 \text{ Am}^{-2} = 3100 \text{ Amm}^{-2}$.

- Referring to slide 12 of lecture 1 or slides 41-43 of lecture 2, this value is not unreasonable.
- Actually, what we calculated is the engineering current density J_e in the wire as a whole, rather than the critical current density J_c in the filaments (see slide 34, lecture 1).

The ‘error’ that we made is in the volume-normalization we made in problem 1a to go from magnetic moment m to magnetization M . If we only consider the hysteretic magnetization², the magnetic moment m of the sample is a superposition of the N magnetic moments m_f of the individual filaments. The hysteretic magnetization resides in the filaments and we ‘should’ have normalized by the filamentary volume $V_f = \lambda V$ instead of by the wire volume V .

If we would have done this, we would have arrived at the critical state expression $J_c = \frac{3\pi \Delta m}{4 V_f} \frac{1}{d_f}$

rather than, as we did, $J_e = \frac{3\pi \Delta m}{4 V} \frac{1}{d_f} = \lambda \left(\frac{3\pi \Delta m}{4 V_f} \frac{1}{d_f} \right) = \lambda J_c$.

¹ In an actual measurement – as opposed to in the critical state theory – the magnitude of the magnetization for increasing field and for decreasing field is rarely the same, i.e. $|M_+| \neq |M_-|$. This may be partly due to the “reversible” component of the magnetization (the diamagnetic response of a superconductor which is always present, regardless of the flux pinning which causes the hysteresis) and partly to instrumental factors (offsets). By calculating the irreversible component $\Delta M = M - M_+$ of the magnetization we effectively eliminate these contributions and regain correspondence between experiment and theory.

² i.e. if we neglect for the time being the coupling currents in the matrix, that will be considered in problem 1c.

Nevertheless, in the context of AC losses it is customary to normalize with the whole sample volume rather than just the filamentary volume. The loss density measured on single wires (in Jm^{-3}) then corresponds to the average loss in the whole wire, so that e.g. a magnet designer 'simply' needs to work out the field distribution throughout the coil winding pack and then can integrate the measured or calculated losses for given fields and ramp rates to obtain the overall heat load on his/her device (see slides 27-30, lecture 5).

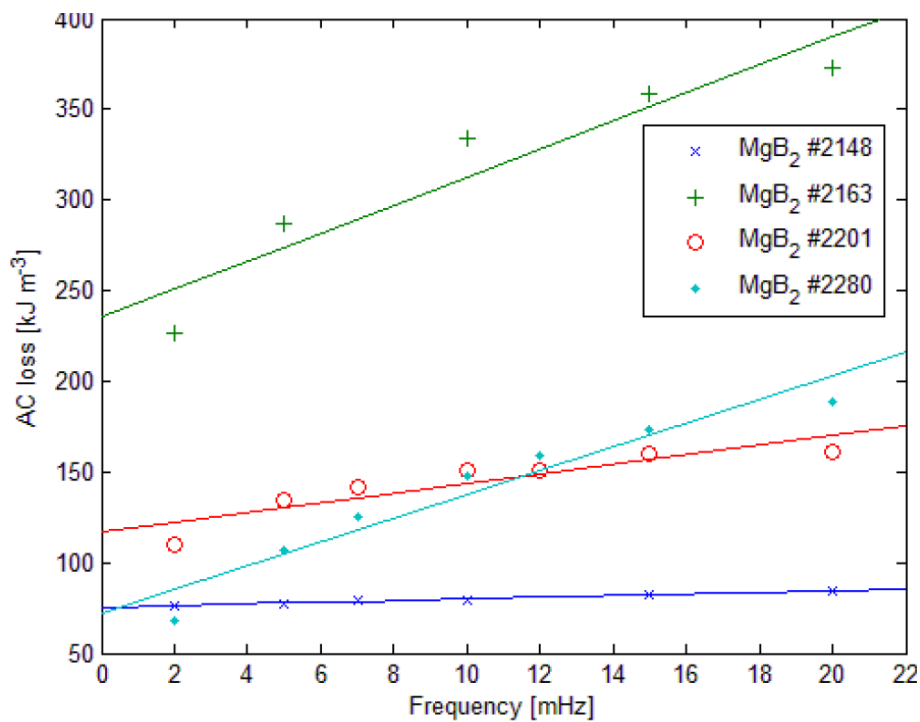


Figure 2: Frequency dependence of the magnetization losses in 4 different prototype MgB_2 wires, measured cycling between 1 and 3T at $T = 4.2\text{K}$.

Figure 2 shows the ramp-rate dependent losses in the four wires described below. The straight lines fitted through the data points represent a relation discussed in the lecture. (*Which one?*)

The straight lines have an offset (their intercept with the y-axis) and a slope. The offset value corresponds to the hysteresis loss discussed in problem 1a, which is frequency-independent. The excess value above this offset corresponds to the coupling losses, which initially increase linearly with frequency (relations on slides 21-22, lecture 5).

Question 1c)

- With the aid of figure 2, estimate the time constant τ of the coupling loss in wire #2163.

We will use the relation $P_c = \frac{2}{\mu_0} \lambda \lambda_{fb} \dot{B}^2 \tau$ (slide 23, lecture 5³).

³ The cable fill factor λ_c is in these single-wire measurements irrelevant, the wire fill factor λ_w is in our notation simply λ .

Figure 2 shows loss density per cycle Q_c [Jm^{-3}] as function of frequency f [Hz] rather than power density P_c [Wm^{-3}] vs. ramp rate \dot{B} [Ts^{-1}], so we need to convert between both. This is easily done by noting that $P_c = Q_c f$ and $\dot{B} = 2\Delta B f$, with $\Delta B = 2\text{T}$ the peak-to-peak amplitude of our field loops:

$Q_c = \frac{8}{\mu_0} \lambda \lambda_{fb} (\Delta B)^2 f \tau$. Differentiating with respect to f yields the slope of the curves in figure 2,

$$\frac{dQ_c}{df} = \frac{8}{\mu_0} \lambda \lambda_{fb} (\Delta B)^2 \tau, \text{ which is rearranged to } \tau = \frac{\mu_0}{8 \lambda \lambda_{fb} (\Delta B)^2} \frac{dQ_c}{df}.$$

$\lambda_{fb} = \left(\frac{d_{fb}}{d_w}\right)^2$ is the volume fraction of the filamentary zone, where the coupling losses occur (slide

21, lecture 5). Inspection of figure 3 shows that the outer sheath of the wires has a thickness of about $100 \mu\text{m}$, so that $d_{fb} \approx 0.63 \text{ mm}$ and $\lambda_{fb} \approx 0.58$.

Noting that for wire #2163 $Q(f=0) \approx 230 \text{ kJm}^{-3}$ and $Q(f=0.022) \approx 410 \text{ kJm}^{-3}$, we estimate

$$\frac{dQ_c}{df} \approx \frac{(410 - 230) 10^3}{0.022} = 8.2 \text{ MJsm}^{-3}.$$

Filling all this in yields
$$\tau = \frac{4\pi 10^{-7}}{8 \times 0.26 \times 0.58 \times 2^2} \times 8.2 10^6 = 2.1 \text{ s}.$$

- Use your result to estimate the transverse inter-filament resistivity ρ_t (in this particular wire, the filaments are untwisted. In that case one uses half the sample length as an 'effective' twist pitch p).

Here we use the relation $\tau = \frac{\mu_0}{2\rho_t} \left(\frac{p}{2\pi}\right)^2$ (slide 21, lecture 5) or, rearranged, $\rho_t = \frac{\mu_0}{2\tau} \left(\frac{p}{2\pi}\right)^2$.

Setting the twist pitch, as suggested, to half the sample length $p = 0.9 \text{ m}$, we immediately get:

$$\rho_t = \frac{4\pi 10^{-7}}{2 \times 2.1} \left(\frac{0.9}{2\pi}\right)^2 = 6.1 10^{-9} \Omega\text{m}.$$

- Is the value you obtain for ρ_t reasonable compared to typical numbers for metals at low temperature (see previous lectures and problem sessions)?

Yes. The resistivity of Cu at 4.2K typically lies in the range $10^{-12} - 10^{-10} \Omega\text{m}$, depending on the purity, but here we're dealing with Nb diffusion barriers⁴ sheathing the filaments and Monel matrices used to mechanically reinforce the wires and to keep the coupling loss low. Normal state resistivity values for Nb at 4.2K are typically around $\sim 5 10^{-9} \Omega\text{m}$, while the Cu-Ni alloy Monel may have resistivity values in the range $10^{-8} - 10^{-7} \Omega\text{m}$, depending on composition.

⁴ At 4.2K, Nb ceases to be superconducting at fields higher than $\sim 1\text{T}$.

Strand #	# Mono	Barrier	Mono sheath	Multi sheath	additive	dia (mm)	s/c %	sample length (m)
2148†	36	Nb	-	Monel	2%C	0.83	17.1	10
2163	18	Nb	-	Monel	2%C	0.83	25.8	10
2201	6	Nb	Cu	Monel	2%C	0.83	10	10
2280	18	Nb	Monel	Monel	2%C	0.83	9.3	10
2313	1	Nb	Monel	-	2%C	0.83	18.1	10

† strand is twisted at 100 mm pitch

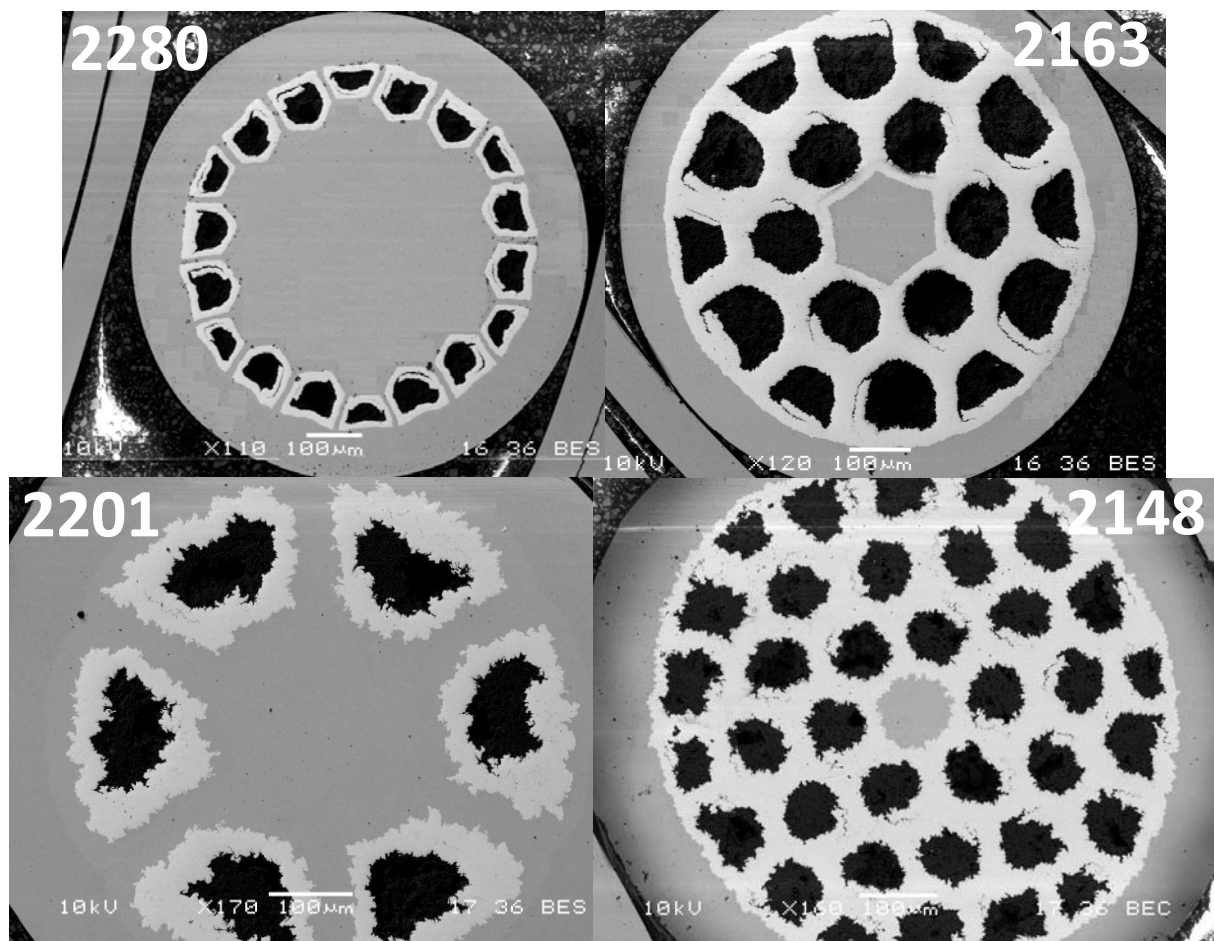


Table 1: Key characteristics of the prototype MgB_2 wires furnished by the producer.

Figure 3: SEM cross-sectional view-graphs of the 4 prototype MgB_2 wires. The darker areas are MgB_2 , the lighter ones Nb and the mid-gray areas copper or Monel (a copper-nickel alloy).

Table 1 and figure 3 provide key characteristics and cross-sectional viewgraphs of 4 of the MgB_2 prototype wires.

Question 1d)

- Still with the aid of figure 2, rank on the one hand the hysteresis loss and on the other the coupling loss in these 4 wires (in other words which wire has the highest loss, which the next-highest, and so on...).

Identifying the hysteresis loss Q_h with the offset $Q(0)$ of the $Q(f) \approx Q(0) + \alpha f$ data and the coupling loss Q_c with the linear extra contribution αf above $Q(0)$ (see also discussion introducing problem 1c), figure 2 clearly shows that:

$$Q_h(\#2280) \approx 70\text{kJm}^{-3} < Q_h(\#2148) \approx 75\text{kJm}^{-3} < Q_h(\#2201) \approx 120\text{kJm}^{-3} < Q_h(\#2163) \approx 230\text{kJm}^{-3};$$

and⁵

$$Q_c(\#2148) \approx 10\text{kJm}^{-3} < Q_c(\#2201) \approx 60\text{kJm}^{-3} < Q_c(\#2280) \approx 150\text{kJm}^{-3} < Q_c(\#2163) \approx 180\text{kJm}^{-3}.$$

- Comment on these 2 rankings using the information provided by table 1 and figure 3.

Hysteresis losses are determined by filament size and J_c -value. With the earlier discussed formula

$$d_f = \sqrt{\frac{\lambda}{N}} d_w \quad (\text{see problem 1b}) \text{ and the data from table 1, we calculate}$$

$$d_f(\#2148) = 57\mu\text{m} < d_f(\#2280) = 60\mu\text{m} < d_f(\#2163) = 99\mu\text{m} < d_f(\#2201) = 107\mu\text{m}.$$

The correlation between Q_h and d_f is reasonable for wires #2148, #2280 and #2201: we may conclude that they have similar J_c -values and that differences in their hysteresis losses are mainly determined by differences in filament size. #2163 is the odd one out. It has a somewhat lower filament size than #2201 but nearly double its hysteresis loss. The only explanation for this is a significantly higher J_c -value. This is corroborated by a visual inspection of the MgB_2/Nb interface of this wire, which is noticeably smoother than in the other wires. This might suggest a cleaner microstructure and/or finer grain size inside the filaments and hence a higher J_c -value (see lecture 1).

In terms of coupling losses, wire #2148 is the only one with twisted filaments ($p = 0.1\text{m}$ instead of 0.9m) and clearly has much lower coupling loss than the others. Wire #2163 offers a continuous Nb path for the coupling currents and indeed has somewhat higher coupling loss than #2280, there coupling currents need to pass (higher resistivity) Monel layers. Here, the odd one out is #2201. It has a pure Cu central region (the lightest gray area in the micrograph, see also table 1) and thus should have the highest coupling losses, but Q_c for this wire is actually lower than #2163 and #2280. The reason for this anomalous behavior is not clear.

⁵ The coupling loss contribution is evaluated at 22mHz.

Appendix B

Data Extraction for Numerical Model

```
1 %% Load NMT or IT machine
2 if exist('Hxx1')==0 % skip if data is loaded
3     model = mphload('IT_rot-stator'), p=18; alpha=42; dset='dset8';
4 %     model = mphload('NMT_rot-stator'), p=11; alpha=38; dset='dset7';
5 end
6 %% load variables
7 f = 9.65/60; % rotational speed [Hz]
8 p_steps = 900; r_steps = 10; % angular and radial steps
9 p1 = (0:1/p_steps:1)*pi/p; % angle array of boundary 1 and 3
10 p2 = (180-alpha)/180*pi/p; % angle of boundary 2
11 p4 = alpha/180*pi/p; % angle of boundary 4
12 r1 = 2460; r3 = 2450; % radius of boundary 1 and 3
13 r2 = r3 : 10/r_steps : r1; % radial array of boundary 2 and 4
14 t = 0 : 1/(f*p*100) : 2/(f*p); % time array1.
15
16 % create coordinate array of each boundary
17 xy1 = [cos(p1).*r1 ; sin(p1).*r1]; xy2 = [cos(p2).*r2 ; sin(p2).*r2];
18 xy3 = [cos(p1).*r3 ; sin(p1).*r3]; xy4 = [cos(p4).*r2 ; sin(p4).*r2];
19
20 % extract data for all time steps and field angles, skip first time step
21 if exist('Hxx1')==0 % skip if data is loaded
22     [Hxx1,Hyy1] = mphinterp(model,{'rmm.Hx' 'rmm.Hy'},'coord',xy1,'solnum
23     ',2:1:202,'dataset',dset,'outersolnum','all');
24     [Hxx2,Hyy2] = mphinterp(model,{'rmm.Hx' 'rmm.Hy'},'coord',xy2,'solnum
25     ',2:1:202,'dataset',dset,'outersolnum','all');
26     [Hxx3,Hyy3] = mphinterp(model,{'rmm.Hx' 'rmm.Hy'},'coord',xy3,'solnum
27     ',2:1:202,'dataset',dset,'outersolnum','all');
28     [Hxx4,Hyy4] = mphinterp(model,{'rmm.Hx' 'rmm.Hy'},'coord',xy4,'solnum
29     ',2:1:202,'dataset',dset,'outersolnum','all');
30     fprintf('data loaded')
31 end
32 %% post-processing
33 for k=1:11 % process each field angle separately
```

```

30 Hx1 = Hxx1(:, :, k); Hy1 = Hyy1(:, :, k);
31 Hx2 = Hxx2(:, :, k); Hy2 = Hyy2(:, :, k);
32 Hx3 = Hxx3(:, :, k); Hy3 = Hyy3(:, :, k);
33 Hx4 = Hxx4(:, :, k); Hy4 = Hyy4(:, :, k);
34
35 % reshape for correct matrix multiplication
36 l_p = length(p1); l_t = length(t); l_r=length(r2);
37 Hx1 = reshape(Hx1.', l_p, l_t); Hy1 = reshape(Hy1.', l_p, l_t);
38 Hx2 = reshape(Hx2.', l_r, l_t); Hy2 = reshape(Hy2.', l_r, l_t);
39 Hx3 = reshape(Hx3.', l_p, l_t); Hy3 = reshape(Hy3.', l_p, l_t);
40 Hx4 = reshape(Hx4.', l_r, l_t); Hy4 = reshape(Hy4.', l_r, l_t);
41
42 % rotate coordinate system by multiplying with rotation matrix
43 for i=1:l_p % transform boundary 1 and 3
44     rot_mat = [cos(-p1(i)) -sin(-p1(i));...
45               sin(-p1(i))  cos(-p1(i))];
46     rot1 = rot_mat * [Hx1(i, :) ; Hy1(i, :)];
47     rot3 = rot_mat * [Hx3(i, :) ; Hy3(i, :)];
48     Hr1(:, i, k) = rot1(1, :); % radial field component
49     Ht1(:, i, k) = rot1(2, :); % tangential field component
50     Hr3(:, i, k) = rot3(1, :); % radial field component
51     Ht3(:, i, k) = rot3(2, :); % tangential field component
52 end
53 for i=1:l_r % rotate boundary 2 and 4
54     rot_mat = [cos(-p2) -sin(-p2) ; sin(-p2)  cos(-p2)];
55     rot2 = rot_mat * [Hx2(i, :) ; Hy2(i, :)];
56     rot4 = rot_mat * [Hx4(i, :) ; Hy4(i, :)];
57     Hr2(:, i, k) = rot2(1, :); % radial field component
58     Ht2(:, i, k) = rot2(2, :); % tangential field component
59     Hr4(:, i, k) = rot4(1, :); % radial field component
60     Ht4(:, i, k) = rot4(2, :); % tangential field component
61 end
62 end
63 %% filter
64 Ht_fft1 = fft(Ht1); Ht_fft2 = fft(Hr2); % transform to frequency domain
65 Ht_fft3 = fft(Ht3); Ht_fft4 = fft(Hr4); % transform to frequency domain
66 Ht_fft1(51:152, :, :) = 0; Ht_fft2(51:152, :, :) = 0; % remove high f
67 Ht_fft3(51:152, :, :) = 0; Ht_fft4(51:152, :, :) = 0; % remove high f
68 Ht_ifft1 = ifft(Ht_fft1); Ht_ifft2 = ifft(Ht_fft2); % back to time domain
69 Ht_ifft3 = ifft(Ht_fft3); Ht_ifft4 = ifft(Ht_fft4); % back to time domain
70
71 %% create data for look up function (LUF)
72 [t1, phi11] = ndgrid(t, p1); [t2, r22] = ndgrid(t, r2); % create grid
73 [t3, phi33] = ndgrid(t, p1); [t4, r44] = ndgrid(t, r2); % create grid
74
75 for i=1:11 % make smooth function out of data
76     F_Ht1 = griddedInterpolant(t1, phi11, Ht_ifft1(:, :, i), 'spline');
77     F_Ht2 = griddedInterpolant(t2, r22, Ht_ifft2(:, :, i), 'spline');
78     F_Ht3 = griddedInterpolant(t3, phi33, Ht_ifft3(:, :, i), 'spline');
79     F_Ht4 = griddedInterpolant(t4, r44, Ht_ifft4(:, :, i), 'spline');
80     file=['IT_Ht_data_winding_la', num2str(i), '.mat'];
81     save(file, 'F_Ht1', 'F_Ht2', 'F_Ht3', 'F_Ht4') % store data
82 end

```

Appendix C

Example of Publication

AC Loss Modeling of Superconducting Field Windings for A 10MW Wind Turbine Generator - an Analytical and Numerical Approach

J. Schellevis, D. Liu, H. Polinder

Abstract—One of the promising drive train topologies currently being investigated is the direct drive superconducting wind turbine drive train. This configuration allows for higher reliability, less top mass and nearly full independence of the volatile market of rare earth metals. Thermal budgets are very important in designing a superconducting generator. This paper discusses an analytical and numerical method of estimating the AC-loss in a type-II superconducting field winding of two designs of a 10MW wind turbine generator at steady state.

Index Terms—AC loss, Analytical modeling, Numerical modeling, Superconducting generator, Wind turbine

I. INTRODUCTION

SIZES of wind turbines are ever since increasing in size, mass and costs. A superconducting direct drive wind turbine can reduce the weight and structural costs of the turbine due to the smaller volume of the generator compared to conventional direct drive generators. Additionally, the superconducting generator makes almost no use of rare earth materials which removes a major uncertainty in material costs.

AC losses in superconducting windings are difficult to predict but are very important to the design of the cooling system. Minimized AC losses can reduce the initial and operational costs of a superconducting generator since the capacity of the cryo-cooler can be minimal and the required cooling power is minimal, which is the AC loss times a factor of 100 due to the low Coefficient of Performance (CoP).

This paper describes an analytical method for AC loss estimation in superconducting MgB_2 field windings. Also a numerical model of the superconductor winding is derived. Both methods are applied on two partially superconducting generator designs, one with Non Magnetic armature Teeth (NMT) and one with Iron armature Teeth (IT) shown in Figure 1 and 2.

Section II discusses the analytical equations and methods followed by the introduction of the numerical model in Section III. Then, Section IV shows the results of the analytical and numerical modeling of a 10MW superconducting generator followed by the conclusions in Section V.

II. ANALYTICAL MODELING

A. AC loss mechanisms

A multifilamentary superconducting wire usually consists of multiple types of materials. In this project the multifilament MgB_2 is embedded into an Ni matrix which is pressed on a copper stabilizer strip as is shown in Figure 3.

Each material in the wire is prone to a different type of AC loss mechanism. The following loss mechanism are present:

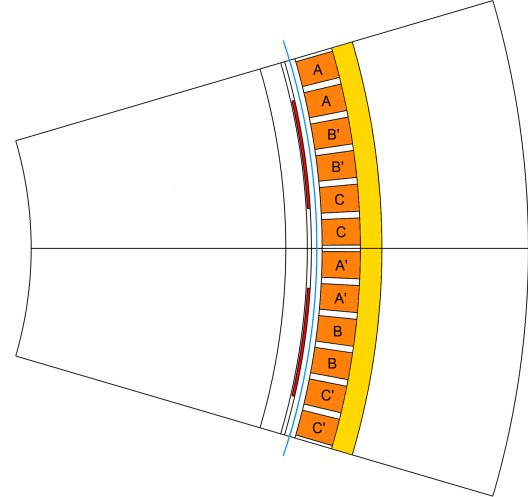


Fig. 1. Cross section of pole pair of NMT machine design.

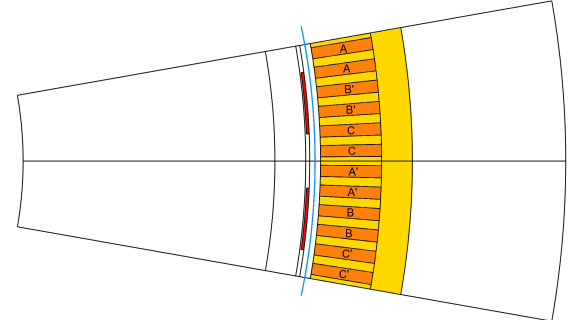


Fig. 2. Cross section of pole pair of IT machine design.

- Hysteresis loss
Caused by movement of magnetic flux lines in the superconductor.
- Eddy current loss
Caused by induced currents in the normal metal of a wire due to changing magnetic field.
- Coupling loss
Caused by cross-over currents from one filament to the other, through the normal metal regions of a wire.
- Ferromagnetic loss
Caused by hysteric behaviour of ferromagnetic non-superconducting materials of a wire.

In AC loss calculations, an important factor is the relative penetration field which is in the case of cylindrical filaments defined as

$$\beta = \frac{B_0}{B_p} = \frac{H_0}{H_p} \quad (1)$$

$$H_p = \frac{2}{\pi} a j_c = \frac{B_p}{\mu_0} \quad (2)$$

where a is the radius of the superconductor and j_c the critical

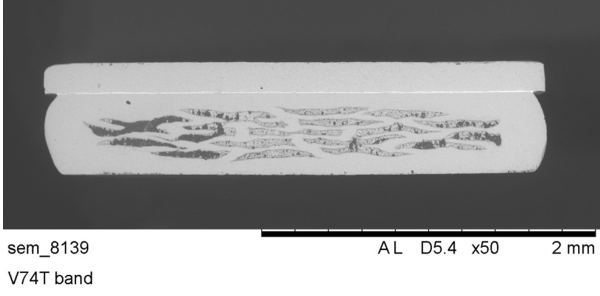


Fig. 3. Cross section of superconducting wire with 19 MgB₂ filaments embedded in a nickel matrix with a copper stabilizer strip on top.

current density.

The hysteresis loss per unit volume in a multifilamentary superconducting wire can be calculated with

$$\frac{\bar{P}_h}{V} = \lambda f \frac{16}{3\pi} j_c a \mu_0 H_0 \quad (3)$$

$$\frac{\bar{P}_h}{V} \approx \lambda f \frac{256}{9\pi} \frac{\mu_0 H_0^3}{2a j_c} \quad (4)$$

$$\frac{\bar{P}_h}{V} = \lambda f \frac{4}{3} \mu_0 [3H_0 H_p - 2H_p^2] \quad (5)$$

$$\frac{\bar{P}_h}{V} = \lambda f \frac{4}{3} \mu_0 \frac{H_0^3}{H_p} \quad (6)$$

Eq. 3 and 4 are applicable on cylindrical filament geometries at $\beta > 1$ for the first equation and $\beta < 1$ for the latter. Eq. 5 and 6 are valid for rectangular geometry filaments with the boundary condition of $\beta > 1$ for the first equation and $\beta < 1$ for the latter. V is the volume of the wire, λ is the superconductor fill factor, f and H_0 are the frequency and amplitude of the externally applied magnetic field.

The eddy current loss per unit volume in a solid rectangular wire in perpendicular magnetic field is described by [1]

$$\frac{P_e}{V} = (\pi f \mu_0 H_0 a)^2 \frac{\sigma_{nm}}{6} \quad (7)$$

where σ_{nm} is the conductivity of the normal metal stabilizer strip.

The coupling loss can be calculated with [2]

$$\frac{\bar{P}_c}{V} = (2\pi f)^2 \frac{\sigma_{\perp} (\mu_0 H_0)^2}{2} \left[\left(\frac{L}{2\pi} \right)^2 + \frac{a_0^2}{4} \right] \quad (8)$$

$$\sigma_{\perp} = \sigma_m \frac{(1 - \lambda)}{1 + \lambda} \quad (9)$$

where σ_{\perp} is the perpendicular conductivity of the filamentary region which needs to be estimated according to the "anisotropic continuum" model [3]. In the case of high electrical conductivity matrix material like nickel and no filament insulation σ_{\perp} can be described, to good approximation with Eq. 9

Ferromagnetic loss per unit volume can be estimated with [4]

$$\frac{P_f}{V} = \lambda_{fer} f K_h B_{max}^n \quad (10)$$

where λ_{fer} is the fill factor of the ferromagnetic material and K_h is a constant depending on volume and type of material. n is an exponent which can vary from 1.5 to 2.5 and needs to be empirically determined. K_h and n are not known for the wire of this project and therefore the ferromagnetic loss is not further evaluated.

B. Frequency and Amplitude Determination

The source of AC loss in the field windings are time and space harmonics. The time harmonics are caused by the connected armature power electronics and will be absorbed for over 98% in a 10mm thick Electro Magnetic (EM) shield applied on the rotor. The space harmonics are assumed to be unaffected by the EM shield.

The space harmonics in the machine are determined with numerical modeling where the field and armature windings are given a uniform current density boundary condition. The solve field distribution over time is evaluated throughout the field winding and used as input for the analytical calculations.

The equations are only valid for single frequency signals, thus a dominant frequency selection method is derived which selects the largest AC loss contribution in the frequency spectrum of the space harmonics. Either the sixth or the twelfth harmonic frequency is dominant and can be selected with

$$f = f_6 \left[\frac{3}{2} + \frac{1}{\pi} \arctan(2 \times 10^3 \kappa) \right] \quad (11)$$

$$\kappa = \frac{C_c}{C_h} f_6 (4\hat{H}_{12}^2 - \hat{H}_6^2) + 2\hat{H}_{12} - \hat{H}_6 \quad (12)$$

where κ is value which is positive if the loss contribution of the twelfth harmonic frequency is dominant and is negative when the sixth harmonic frequency is dominant.

The amplitude of the external field is determined with

$$H_{peak-rms} = \sqrt{2} \sqrt{\frac{1}{F_s t_p} \sum_{t=0}^{t_p} H(t)^2} \quad (13)$$

where F_s is the sample frequency of the time dependent data t_p is the elapsed time after the rotation of one pole and t is the time.

III. NUMERICAL MODELING

The numerical modeling is done with Comsol Multiphysics (®). Since the electric field in a superconductor is depending on the current density a circular dependency arises when using the standard Magnetic Field physics supplied by Comsol. Therefore the superconductor model makes use of the Magnetic field formulation physics where Faraday law can be adapted to use the E(J) curve, defined in the material properties with

$$\mathbf{E}(\mathbf{J}) = E_0 \left(\frac{|\mathbf{J}| - J_c}{J_c} \right)^\gamma \frac{|\mathbf{J}|}{\mathbf{J}} \quad (14)$$

where E_0 and γ are constants used for fitting the E(J) curve to the measured E(J) results. This approach is based on a suggestion by Brambilla [5].

Since this approach will solve the current density distribution in the field winding, this has to be the free variable. Therefore the magnetic field distribution at the boundary of the field winding is copied from a different model where the field distribution is determined base on uniform current densities trough the windings.

All calculations are done in the time domain and for different angles between rotor and armature field, changing the operational torque with increasing field angle.

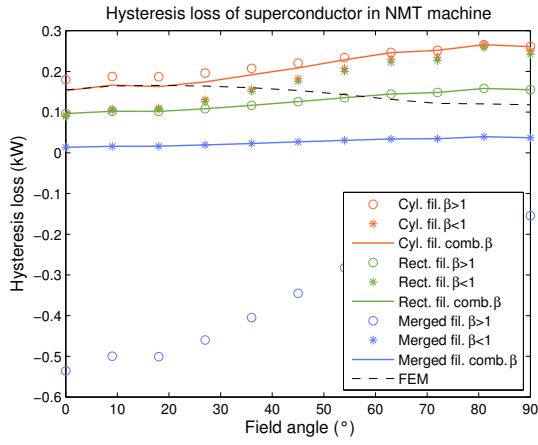


Fig. 4. Hysteresis loss in the AT machine as function of the field angle

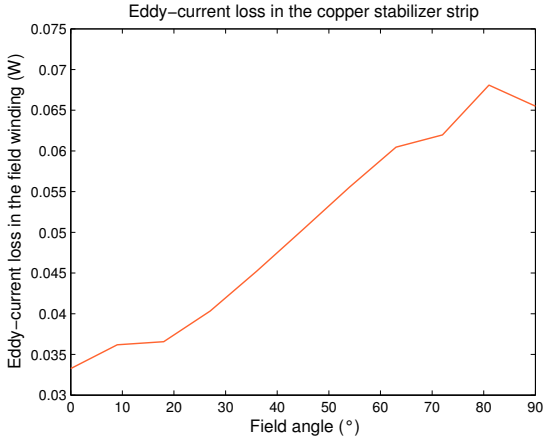


Fig. 5. Eddy current loss in the AT machine as function of the field angle

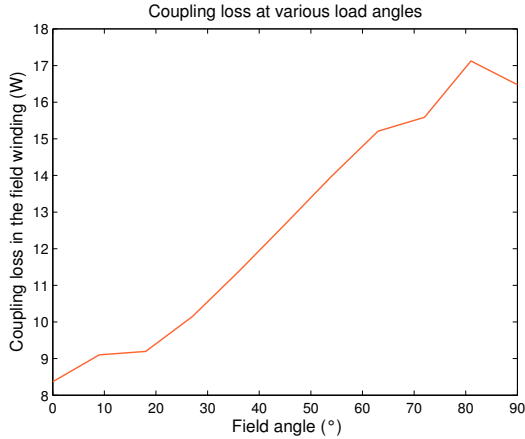


Fig. 6. Coupling loss in the AT machine as function of the field angle

IV. RESULTS

Figure 4, 5 and 6 show the total hysteresis, eddy current and coupling loss in the field winding of the NMT machine. The hysteresis loss in the NMT machine, is increasing with the field angle and ranging from 13.7W up to 266W depending on the assumed filament geometry. The absolute value of the numerically calculated loss is ranging from 118W to 166W which is in the same range as the analytical results. The difference is caused by assuming different filament geometries and therefore different penetration fields. The FEM model assumes a fully coupled winding which results in a different current distribution than was applied in the analytical calculations.

The eddy current loss result shows the frequency of the space harmonics is low enough for neglecting this loss contribution. The coupling loss is responsible for about 5% of the total loss in the cylindrical filament scenario and up to 36% of the total loss in merged filament scenario and therefore has to be considered in accurate AC loss estimations.

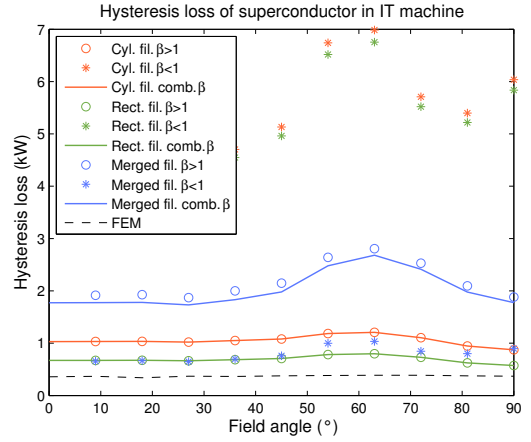


Fig. 7. Hysteresis loss in the IT machine as function of the field angle

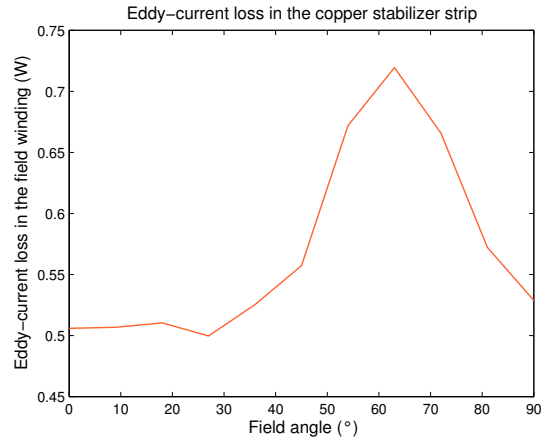


Fig. 8. Eddy current loss in the IT machine as function of the field angle

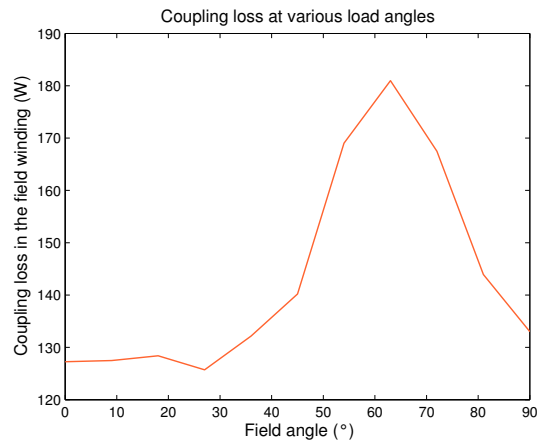


Fig. 9. Coupling loss in the IT machine as function of the field angle

The total hysteresis, eddy current and coupling loss of the IT machine are shown in Figure 7, 8 and 9. The AC loss in the IT machine is much larger compared to the NMT machine. This is caused by the larger space harmonics at higher frequencies caused by the low reluctance teeth, concentrating the magnetic field. The hysteresis loss for the various scenarios is ranging from 570W to 2.68kW and the

numerical result is a bit lower, ranging from 341W to 387W. The FEM result of the IT machine is on average 2.5 times larger compared to the NMT machine.

The eddy current loss is with less than 0.1% of the total loss, also negligible in this machine. The coupling loss is producing 5% up to 14% of the total AC loss.

V. CONCLUSIONS

AC losses in field windings of an electrical machine originate from four macroscopic loss mechanisms: hysteresis loss, eddy current loss, coupling loss and ferromagnetic loss.

The hysteresis loss derived from analytical calculations is in the same order as the numerically calculated hysteresis loss. The iron teeth design of a 10MW superconducting wind turbine experiences much larger AC losses in the field windings compared to a similar machine with non-magnetic teeth. The analytical and numerical results show a difference of 2.5 to 10 times larger AC loss in the IT machine.

The eddy current loss in the field windings of a direct drive superconducting wind turbine can be neglected due to the low frequency of the space harmonics. Coupling loss has to be evaluated for accurate loss estimation since the results show a coupling loss contribution ranging from 5% to 36% to the total AC loss.

REFERENCES

- [1] F. Fiorillo, *Characterization and Measurement of Magnetic Materials*, 1st ed. Amsterdam: Elsevier B.V., 2004.
- [2] W. J. J. Carr, *AC loss and macroscopic theory of superconductors*. London [etc.]: London etc. : Taylor & amp, 2001.
- [3] W. Carr, "Electromagnetic theory for filamentary superconductors," *Physical Review B*, vol. 11, no. 4, pp. 1547–1554, Feb. 1975. [Online]. Available: <http://link.aps.org/doi/10.1103/PhysRevB.11.1547>
- [4] P. C. Sen, *Principles of electric machines and power electronics*. New York [etc.]: New York etc. : Wiley, 1997.
- [5] Comsol Multiphysics, "Superconducting Wire - COMSOL," p. 12, 2014. [Online]. Available: <http://www.comsol.com/model/superconducting-wire-689>